Deep–Sea Research I 228 (2026) 104650

Contents lists available at ScienceDirect

Deep-Sea Research Part I

journal homepage: www.elsevier.com/locate/dsri

MARS lander: Georeferencing landing and pop points of untethered ocean monitoring systems using fundamental physics

Marko Radeta [a,b,c,g,*], Zahra Behboodi [a], Vladimir Zekovic [c,d], Décio Alves [e], David Pestana [h], Daniel Nunes [h], Margarida Freitas [i], Ankit Gupta [a,e,l], João Pestana [a,b,g], Dinarte Vieira [a,b,g], Sílvia Almeida [b,g], Morgado Dias [e], João Canning Clode [b,f,g], Rui Caldeira [j], Paulo Relvas [k], Antonio Vasiljevic [m]

[a] *Wave Labs, Faculty of Exact Sciences and Engineering, University of Madeira, Portugal*
[b] *MARE - Marine and Environmental Sciences Centre, ARNET - Aquatic Research Network, Agência Regional Agency for Research, Technology and Innovation Development (ARDITI), TECNOPOLO, Madeira Science and Technology Center, Floor -2, Office: 2. Caminho da Penteada, 9020-105 Funchal, Madeira, Portugal*
[c] *Department of Astronomy, Faculty of Mathematics, University of Belgrade, Serbia*
[d] *Department of Astrophysical Sciences, Princeton University, NJ, USA*
[e] *University of Madeira and Interactive Technologies Institute (ITI/LARSyS), ARDITI, Portugal*
[f] *Smithsonian Environmental Research Center, Edgewater, MD, USA*
[g] *Faculty of Life Sciences, University of Madeira, Portugal*
[h] *Instituto Superior Técnico (IST), University of Lisbon, Portugal*
[i] *Faculty of Engineering, University of Porto, Portugal*
[j] *Observatório Oceânico da Madeira (OOM), ARDITI, Madeira, Portugal*
[k] *CCMAR (Centre of Marine Sciences), University of Algarve, Portugal*
[l] *Department of Biomedical Engineering and Cybernetics, Faculty of Electrical Engineering and Computer Science, VSB-Technical University of Ostrava, Czechia*
[m] *Department of Marine Technology, Norwegian University of Science and Technology (NTNU), Trondheim, Norway*

ARTICLE INFO

Keywords:
Upper ocean dynamics
Ocean physics
Dead reckoning
Water column monitoring
Underwater trajectories
Radial excursion prediction
Low-cost landers
Hydrodynamics
Numerical simulations
Lander geometry

ABSTRACT

Subsurface observations are crucial for understanding the ocean's role in Earth's climate and for refining climate models. However, existing aquatic monitoring systems that allow such insights remain complex and costly due to their high demands for deployment, sampling, and recapture. Since low-cost, easy-to-deploy deep-sea landers are scarce, and with the aim of facilitating more subsurface observations, this study provides a simple method for georeferencing small-sized untethered landers. Their underwater trajectories are modelled with fundamental physics, dead reckoning, lander geometry, and numerical simulations. Using free fall, upthrust, and ocean current dynamics, the proposed approach estimates their underwater trajectories, including landing (at the seabed) and pop (at the sea surface) points. The method relies on the lander's physical characteristics, including its vertical and horizontal cross-sectional areas, to calculate the drag force coefficients used to determine its trajectories during descent and ascent through the water column. Ocean currents' magnitudes are modelled using Ekman's exponential decay down to 90 m of the water column, while the depths until 900 m are modelled from prior ADCP surveys by varying ocean current headings with depth between −20 and 20°. Surface ocean and wind current headings are modelled with open datasets from satellite telemetry. Lander's velocity, displacement, and dive time to the landing and pop points, including the total radial excursion and uncertainty in heading, are analytically derived, numerically calculated, and empirically assessed a-posteriori until 90 m, yielding a ∼38 m radial excursion (40% error) against the obtained GNSS coordinates in field deployment, and 33° in heading uncertainty during a 138-s excursion. Additional random walk simulations are shown for full ocean depth obtaining radial excursion of 1038 m with 278 min total dive time. This approach is generalizable to any subsurface aquatic monitoring systems targeting deployments with diverse payloads from smaller sea vessels, not requiring cranes, radio, GNSS, or acoustic telemetry. Since it accounts for key nature factors, our method provides special benefits in planning and optimizing deployments. Additional discussion focuses on the method's practicality for full ocean depth deployments.

---

[*] Corresponding author. Wave Labs, Faculty of Exact Sciences and Engineering, University of Madeira, Portugal.
E-mail address: marko@wave-labs.org (M. Radeta).

https://doi.org/10.1016/j.dsr.2026.104650
Received 14 April 2025; Received in revised form 28 December 2025; Accepted 3 January 2026

1. Introduction

Subsurface ocean observation is critical to understanding the ocean's functioning as a whole (Gould et al., 2013). While the ocean surface is continuously monitored through remote sensing techniques based on satellites (Ardhuin et al., 2018), planes (Rascle et al., 2020), drones (Monteiro et al., 2021), and others, sampling the essential ocean variables, including observations of the ocean water column and near-bottom characteristics, remains sparse (Liu et al., 2020). Indeed, the most relevant oceanic processes occur in the upper layers, where interaction with the atmosphere determines most of the functioning ecosystem, and rarely in the lower layers, well below the thermocline, and only a fraction of them leave an imprint on the ocean surface (Max et al., 2022). As climate change affects predictable patterns of ocean currents (Miller, 2017) and the dispersal of associated species (García Molinos et al., 2017), more long-term and high-resolution observations of the ocean's interior are needed (Gould et al., 2013).

To gain more insights beneath the ocean surface, hydrodynamic numerical simulations are parametrized, building a suite of models that mimic the ocean behavior (Ramming and Kowalik, 1980), serving as the basis for digital ocean twins development (Rápalo et al., 2024). In terms of hardware, most of the subsurface aquatic monitoring systems include landers and moorings that are used with an integrated large variety of sensors and actuator payloads, as they remain the most cost-effective and long-term candidate for Eulerian observatories (Cristini et al., 2016). Landers carry instruments for scientific sampling (Miwa et al., 2016), ranging from water to environment assessments (Bagley et al., 2004), fauna attraction and trapping (Jamieson, 2016), to gateways (Fukuba et al., 2018) specially used for underwater acoustic communication (Silva et al., 2016). Landers are commonly used for benthic research and can reach full ocean depth (Peoples et al., 2019), such as the Challenger Deep (Jamieson et al., 2009; Muir et al., 2021), while low-cost, easy-to-deploy full ocean depth landers[1] remain scarce.

Landers can be either tethered or untethered, but despite efforts to simplify their deployment (González-Pola et al., 2021), most tethered systems remain costly due to their size and complex logistics. When tethered, an important limiting factor is their umbilical, coaxial, or optical connection to surface vessels (Almeida et al., 2024), which is typically strengthened with synthetic fibers or wound steel layers, allowing landers' mechanical strength to withstand tension as well as real-time data streaming to the surface. However, such tethered connections are prone to entanglement within the ghost gear and require advanced planning, significant logistical efforts, special types of deployment cranes, an experienced crew, and the careful design of their casings (Dominguez-Carrió et al., 2021). In contrast, untethered landers are less costly and can be deployed into the ocean from smaller-sized sea vessels using single-use ballast such as natural cobble (Radeta et al., 2025), reaching terminal velocity[2] during their excursion to the seabed. Depending on their weight, shape, and operational depth, their descent to the seafloor can take up to several hours (Bagley et al., 2004). Once at the seabed, untethered landers typically sample data for several hours, then begin their ascent back to the surface. The ascent starts when the ballast is discarded at the seabed with a timed (Sessions and Marshall, 1971; Heffler and Locke, 1977), galvanic (Jamieson et al., 2013), or surface acoustic (van Haren et al., 2020) signal as a trigger. Lander's gradual ascent is then caused by flotation units in the form of buoys, which cause the (upthrust) buoyancy force.

To increase smaller-sized landers and success in their recapture rate, it is necessary to understand their landing (at the seabed) and pop (at the sea surface) positions (see Graphical Abstract). Prior methods relied either on computational fluid dynamics (Xiang et al., 2020) or on empirical studies mostly conducted in controlled settings such as swimming pools (Yasseri, 2014), yielding the region probabilities of where the sinking objects during descending will touchdown the seabed at a specific distance relative to the drop point (Aanesland, 1987), known as the radial excursion. The same techniques were used for ascending, e.g., when studying how risers may be subject to potential sea vessel collisions (Veritas, 2010) at the sea surface. More accurate landing and pop points can be obtained using controlled descent vehicles with buoyancy engines (Yin et al., 2024), thrusters (Silva et al., 2016), or acoustic pingers (Yang et al., 2022), which transmit the lander's current position to the surface. However, all these approaches suffer from high costs caused by the logistical complexity, availability of resources, and may cause unnecessary stress to marine mammals (Harris et al., 2018). A more affordable approach could leverage dead reckoning with inertial measurement based on sensor fusion of accelerometer, gyroscope, and magnetometer readings (Radeta et al., 2023). However, objects that reach terminal velocity during gradual descent or ascent may exhibit low to almost no acceleration (Equation (A.40) in Appendices). These cause difficulty for algorithms to obtain the correct attitude and heading reference system (Madgwick et al., 2011).

During their descent and ascent, untethered landers are also prone to significant drifts (Berkenpas et al., 2017) caused by the varying horizontal ocean currents (Lewis et al., 2017). Because of this, it is challenging to georeference the landers at the sea surface. Equipping landers with telemetry tools increases their weight, size, logistics, and overall system costs (Silva et al., 2016). This is due to the requirements for battery autonomy and a communication unit for surface telemetry, which can use satellite uplinks or Very High Frequency (VHF) within the line of sight with sea vessels (Schaefer and Fuller, 2016). Cost-effective telemetry can leverage smaller Internet of Things (IoT) hardware and long-range (LoRa) radio to coastal receivers or sea vessels (Radeta et al., 2024). However, it suffers from signal multipath issues caused by water attenuation, proximity to the island peaks, or the absence of a line of sight.

In this context, this study focuses on georeferencing affordable, small-sized untethered landers designed for a lower amount of payloads. Research contributes a model which is validated in situ at the 90 m with additional numerical simulations extending for 900 and 9000 m, facilitating the planning of future lander missions. This approach simplifies logistics, deployment, and recapture operations and allows more subsurface ocean observations.

2. Materials and procedures

The proposed method is based on fundamental physics, lander's geometry, dead reckoning, and numerical simulations, validated theoretically and empirically. The small-sized untethered lander is deployed from a priori known surface (drop) point and depth (obtained from sonar). The overall challenge is predicting its landing and pop points at the seabed and sea surface, respectively (see Graphical Abstract). Lander trajectories during descent and ascent dives are modelled based on their physical characteristics (e.g., cross-sectional area), including the forces and medium acting on it (e.g., weight, buoyancy, drag force, horizontal ocean currents). Numerical simulations with variable ocean currents' magnitudes and headings were computed (as a function of depth) for both shallow and full ocean depth, including the in situ validation in the photic zone.

2.1. Physical characteristics

The untethered benthic lander used in this study (Figs. 1 and 2) is deployed from smaller sea vessels by two persons from the sea surface (drop point) at a predetermined location (using Global Navigation Satellite System–GNSS) and depth (obtained from the sea vessel sonar).

Lander starts its descent dive with free-fall and is subject to

---

[1] An example of the Full Ocean Depth Lander by the Schmid Ocean Institute can be seen at this link: https://schmidtocean.org/technology/robotic-platforms/11000-m-lander/.

[2] A maximum speed attainable by an object during a free-fall through liquid.

horizontal drift caused by ocean currents until reaching the seabed. Once it touches down (landing point), it samples the required data for a custom period, after which it begins its ascent dive to the sea surface. This is caused by the upthrust force from used buoys, the programmable multipurpose auto-release system (Radeta et al., 2025), which ignites the primer at a specific time (Sessions and Marshall, 1971) and releases the natural cobble as a ballast. The challenge is georeferencing the lander at the sea surface when it emerges (pop point) by calculating its radial excursion relative to the drop point.

The lander consists of four different units (Radeta et al., 2025): Buoyancy, Payload–based on Baited Remote Operated Video System-BRUVS (Langlois et al., 2006), Timer, and Ballast (Fig. 3a). Each unit encompasses components approximated to the geometric shapes (Heddleson et al., 1957). For instance, the cobble bottom cross-sectional area was approximated to an ellipse, buoys to circles, and vertical and horizontal supports to long cylinders. The total cross-sectional area A was computed considering both vertical and horizontal displacements, being the most extensive profiles that penetrate the water. The vertical profile during descent (Fig. 3b) included ballast, all buoys, and baited canister as the largest cross-sectional areas, while during ascent, there was no ballast (Fig. 3b). All other components (e.g., double swivels, timers) were considered negligible in causing drag force since they were occluded behind the larger. The horizontal profile during descent and ascent (Fig. 3c) included the vertical frame, bait, and timer.

Since all lander components were assembled from different materials, online product specifications were used to obtain their densities ρ_i (Fig. 4). Each component was measured using callipers and measuring tape, following fundamental principles in metrology, and drawn as 3D models in Autodesk Fusion software to obtain individual volumes V_i and masses $m_i = \rho_i V_i$. Obtained masses and volumes differed for descent (m_{des}, V_{des}) and ascent (m_{asc}, V_{asc}). The details are presented in Table B1 of the Appendices.

This study's tetherless lander setup included the following components: 3 x small and 1 x sizeable deep-sea rated buoys, 1 x vertical and 1 x horizontal support for 1 x rock and 1 x bait canister, respectively joined with 2 x T-connectors, 1 x timer with primer igniter, and 2 x double swivels (see Table B1 in Appendices). To facilitate later analytical derivation, the lander's constant k was computed (Eq. (A.4) as a function of the seawater density ρ_w, the lander's total cross-sectional area A, and the drag force coefficient μ by summing all individual components whose profile penetrates the water during the dive (Fig. 3b and c). The details are presented in Eqs. A.1–A.4 in Appendices.

Four constants were obtained for descent (A_{DES}, μ_{des}), ascent (μ_{asc}, A_{ASC}), and horizontal and vertical axes. The same physical characteristics were also used to obtain the vertical and horizontal terminal velocities of lander dives (Table B2 in Appendices).

$$k(\rho_w, A, \mu) = \frac{1}{2}\rho_w A\mu \quad (kg/m) \tag{A.4}$$

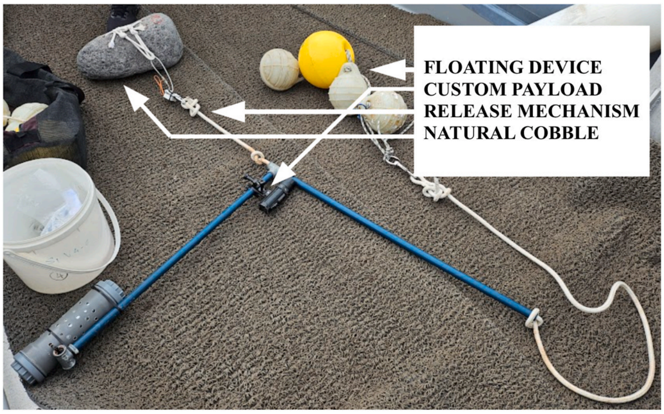

Fig. 1. Untethered MARS lander setup on a sea vessel prior to the deployment at 90 m depth in the south coast of Madeira Island, NE Atlantic. Details of the auto-release system based on natural cobble and DIY timed-release primer ignition are available in Radeta et al. (2025).

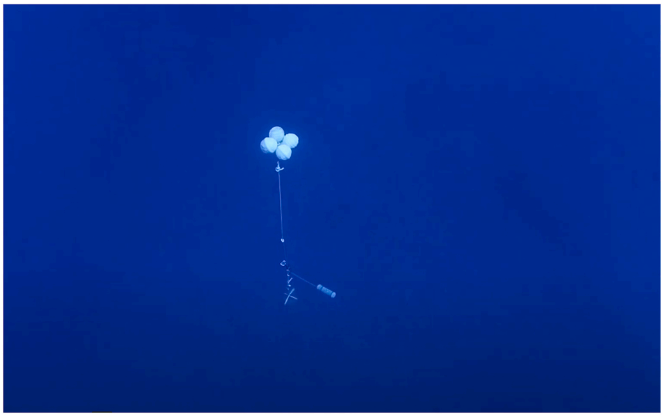

Fig. 2. Untethered MARS lander seen during descent in the water column off the south coast of Madeira Island, NE Atlantic (Radeta et al., 2025).

2.2. *Drop-point fixed coordinate system*

Since this study investigates the lander's underwater trajectories from drop to pop points without angular measurements, a Cartesian coordinate system with three perpendicular axes is suggested, where the origin of the coordinates is at the drop point (a priori known latitude and longitude using a sea vessel GNSS), where the lander is deployed into the water (see Graphical Abstract). The X-axis represents the lander's horizontal displacement and is collinear with the ocean's current heading obtained from the sea vessel, allowing the translation of the coordinate system (Fig. 5). The Y axis represents the lander's heading offset, caused by the ocean current oscillation (see e.g. Fig. 8b). The Z axis represents the lander's vertical displacement and is collinear with the depth, requiring a priori knowledge of the maximum depth Z_{max} using a sea vessel sonar. In this drop-point fixed coordinate system, the Earth's curvature variation is neglected (Bell et al., 2024) as the study focuses on smaller-scale radial excursions. The whole coordinate system is translated in the direction of the radial excursion where the lander emerges (pops) at the sea surface (see Graphical Abstract and Fig. 11d), from which the latitude and longitude are obtained using the geographic coordinate system.

2.3. *Model*

Fundamental physics and Newton's Second Law of Motion are used to compute the forces acting on a lander moving in a fluid, obtaining velocity and displacement during descent and ascent. Fundamental forces acting on the lander are its weight F_W, drag F_D, and buoyancy F_B (Fig. 5). The ocean current in the horizontal direction causes a drag force F_{Dx} to the lander, making it reach the ocean current velocity (v_w) or horizontal terminal velocity, causing motion due to its inertia (see Eq. A.35-A.41 in Appendices). In this model, the damping and added mass as hydrodynamic forces were neglected as the lander uses the open geometry of the structure, moves with low speed without thrusters, and causes laminar motion without turbulence. Also, the vertical component of the ocean currents is neglected as it is commonly much smaller than the horizontal component (Håland et al., 2012).

2.3.1. *Net forces*

In the case of vertical forces, the weight force F_W (N) of an object with mass m (kg) under an acceleration g (m/s^2) due to the gravity pulling the object's mass with a force $F_W = mg$. At the location of study

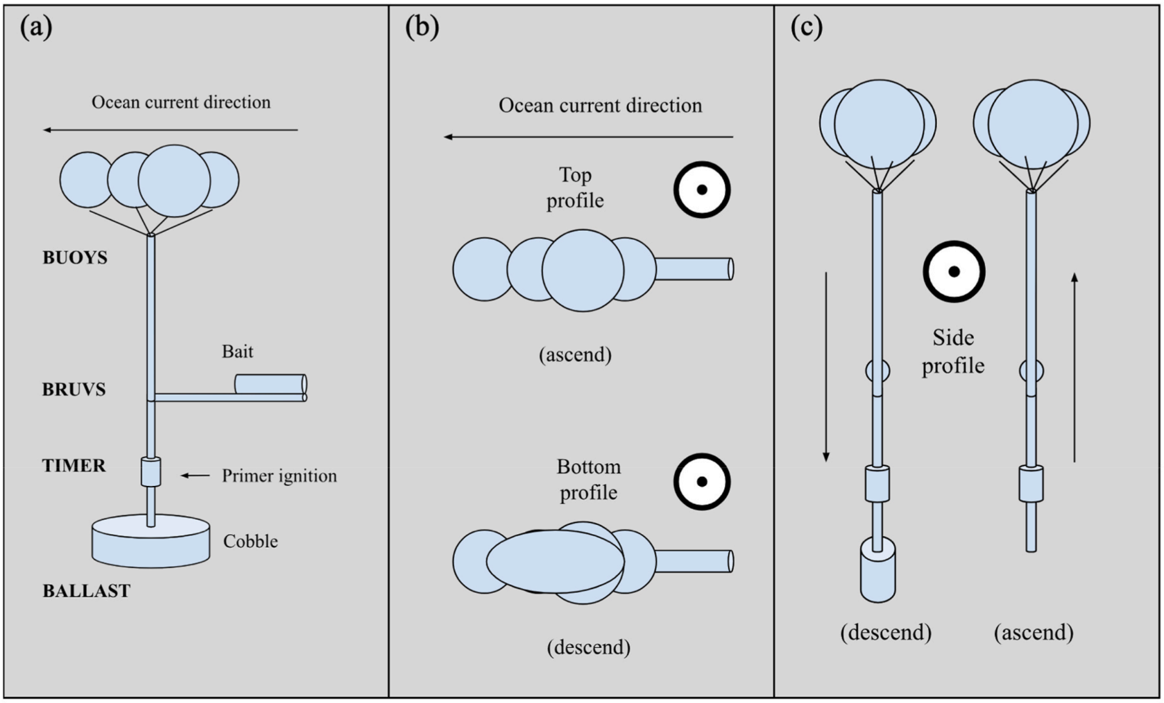

Fig. 3. Schematic of the MARS lander's main units: (a) with cross-sectional areas of vertical (b) and horizontal (c) profiles. A circle with a dot indicates the lander's motion going out of the plane. Details of the auto-release system based on natural cobble and primer ignition are available in Radeta et al. (2025).

deployment latitude, $g = g(0) = 9.7955 m/s^2$ (Moritz, 2000). The buoyant force is $F_B = \rho_w \cdot V \cdot g$ (Munson et al., 2012), where ρ_w is the fluid density. In this study, the considered fluid was seawater with density $\rho_w = 1023.6 kg/m^3$ at a temperature of 25 °C, salinity of 35 g/kg, and 1 atm pressure (Poisson et al., 1980). The V is the volume of displaced fluid equal to the lander's total volume, following Archimedes' principle. The total drag force F_D acting on an object is: $F_D = \rho A \mu v^2 / 2$, where A is the cross-sectional area perpendicular to the fluid's flow (and lander movement), μ is the dimensionless drag force coefficient of fluid resistance on a lander body, and v is the lander's velocity component along the movement direction.

Following Newton's second law, $\overrightarrow{F} = m\overrightarrow{a} = m\frac{d\overrightarrow{V}}{dt} = \sum_{i=1}^{n} \mathbf{F}_i$, with F_i being the sum of the above forces, for a lander in a vertical descent towards the center of gravity, fluid resistance and buoyancy, the net force is $F = F_W - F_B - F_D$. Conversely, for a lander in a vertical ascent towards the sea surface, fluid resistance has the opposite sign $F = F_W - F_B + F_D$. For both descent and ascent, the net forces are non-linear first-order ordinary differential equations (ODEs) seen below, while their derivation is shown in Eqs. A.1–A.3 inside of Appendices.

$$m_{des}g - \rho_w V_{des} g - k_{des} v_{des}^2 = m a_z \tag{A.2}$$

$$m_{asc}g - \rho_w V_{asc} g + k_{asc} v_{asc}^2 = m a_z \tag{A.3}$$

Horizontal force is the drag force caused by the ocean currents, $F_D = \rho_w A \mu / 2$. Vertical velocity and displacement were obtained analytically, allowing the derivation of total lander dive time. Horizontal velocity and horizontal displacement were solved numerically (Eqs A.35–A.42 in Appendices).

Lander's vertical velocity and displacement were derived by summing all the forces being part of the system (Eqs A.11–A.31 in Appendices). Based on its physical characteristics, it is revealed how fast the untethered benthic lander reaches the terminal velocity during both descent and ascent (see Graphical Abstract).

2.3.2. *Terminal velocity*

The lander may experience no acceleration during the dives ($a = 0$), indicating constant velocity. This is also known as the terminal velocity ($v = v_T$), which the lander asymptotically approaches (Afonso, 2008). Naturally, varying ocean currents cause acceleration and deceleration during descent and ascent (Tuchen et al., 2022). The vertical gradients of the horizontal velocity of the ocean current (vertical shear) influence the lander's velocity, which needs to be calculated for the model. Although the terminal velocity v_T is constant, it will differ during ascending and descending. The two terminal velocities (Eq. (A.9) and Eq. (A.10)) differ due to their masses, densities, cross-sectional areas, and drag force coefficients during the descent and ascent (Eqs. A.5–A.10 in Appendices) as the lander's individual components vary between the ascent and descent as the ballast is discarded. The formulae below show the derived terminal velocities during descent and ascent along the Z axis. Obtained vertical terminal velocities of the lander's individual components (Fig. 4) were 1.4 m/s and 1.25 m/s for descent and ascent, respectively.

$$v_{T des} = \sqrt{\frac{m_{des}g - \rho_w V_{des} g}{k_{des}}} \tag{A.9}$$

$$v_{T asc} = -\sqrt{\frac{\rho_w V_{asc} g - m_{asc} g}{k_{asc}}} \tag{A.10}$$

2.3.3. *Vertical velocity*

By solving ODEs from Equations A.2 and A.3 and considering time t as the dive time to the seabed and sea surface, respectively (with t_2 being the start of ascending), the lander's velocity is analytically derived for both descending and ascending, obtaining hyperbolic tangent (Eq. (A.22) and Eq. (A.24)). The corresponding derivation is presented in Eq. A.11–A.15 in Appendices. Vertical velocity during descent and ascent differ in sign and time.

$$v_{z des}(t) = v_{T des} \tanh\left(\frac{k_{des} v_{T des}}{m_{des}} t\right) \tag{A.22}$$

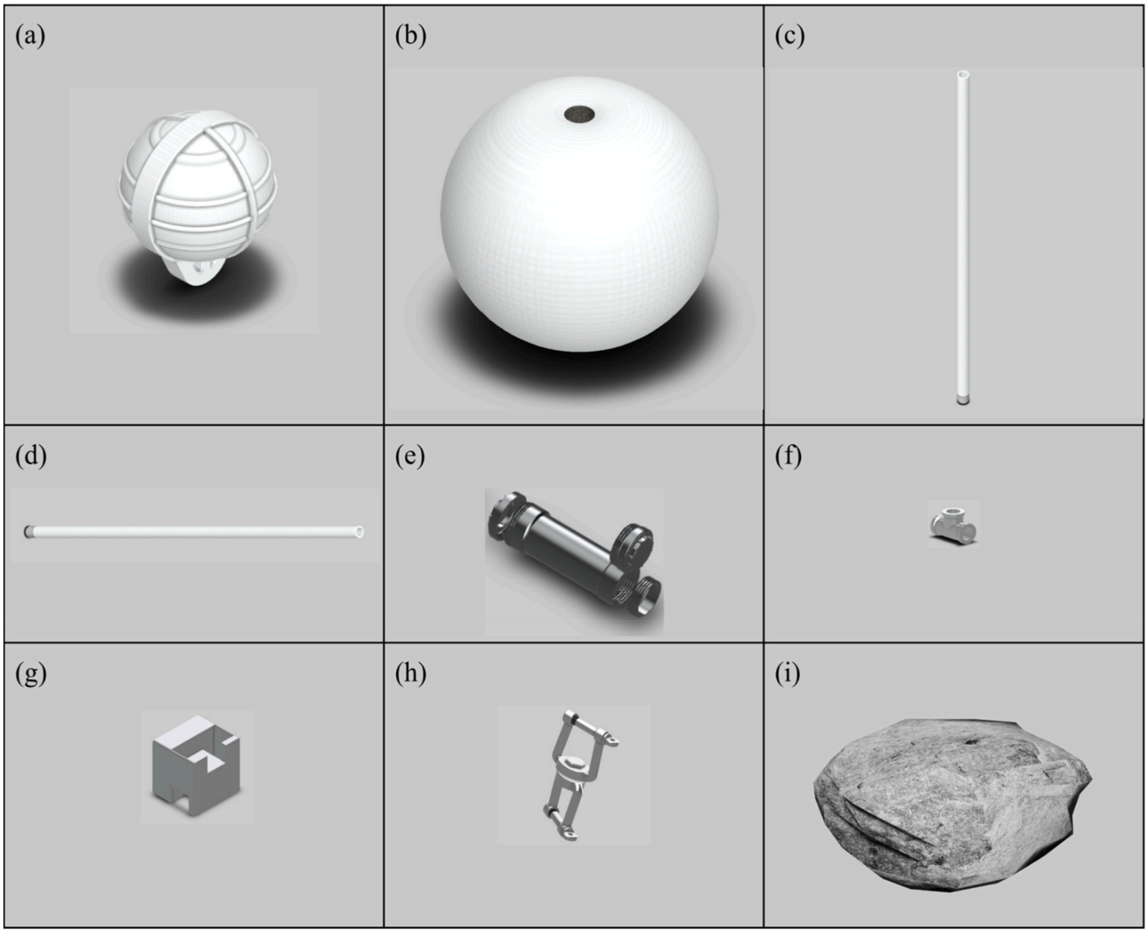

Fig. 4. 3D models of the tetherless MARS lander's individual components and their densities. From left to right: (a) Small Buoy PU (0,289 g/cm^3), (b) Large Buoy HDPE (0,299 g/cm^3), (c) Vertical Support PVC (1,4 g/cm^3), (d) Horizontal Support PVC (1,4 g/cm^3), (e) Bait Canister PVC (1,4 g/cm^3), (f) T-Connection Stainless steel 303 AISI (7,85 g/cm^3), (g) Timer holder PLA (1,32 g/cm^3), (h) Double swivel Stainless steel 303 AISI (7,85 g/cm^3), and (i) Natural Cobble Basalt (2,9 g/cm^3).

$$v_{z_{asc}}(t) = -v_{T_{asc}} \tanh\left[\frac{k_{asc} v_{T_{asc}}}{m_{asc}}(t_2 - t)\right] \tag{A.24}$$

2.3.4. Vertical displacement

From the obtained lander's vertical velocity component v_z, the displacement is integrated along the Z (depth) axis (Eq. (A.30) and Eq. (A.31)). The full derivation is shown in A.25–A.31 inside Appendices and seen in the expression below.

$$z_{des}(t) = \frac{m_{des}}{k_{des}} \ln\left[\cosh\left(\frac{k_{des} v_{T_{des}}}{m_{des}} t\right)\right] \tag{A.30}$$

$$z_{asc}(t) = -\frac{m_{asc}}{k_{asc}} \ln\left[\cosh\left(\frac{k_{asc} v_{T_{asc}}}{m_{asc}}(t_2 - t)\right)\right] + Z_{max} \tag{A.31}$$

2.3.5. Dive time

From vertical displacement, it is possible to obtain the time until touchdown. Lander's mission is divided into three major intervals: descending, data sampling, and ascending, or mathematically: $\Delta t_{TOTAL} = \Delta t_{DES} + \Delta t_{DATA} + \Delta t_{ASC}$. Four important moments are: t_0, indicating the start of the dive (drop point, see Graphical Abstract), t_1 when the lander reaches the targeted seabed depth Z_{max} (landing point, see Graphical Abstract), t_2 when the lander begins its ascent, and t_f when it emerges at the sea surface (pop point, see Graphical Abstract). Additional time may be added until recaptured by the sea vessel. As $t_0 = 0$ is the drop moment, $\Delta t_{TOTAL} = t_f - 0 = t_f$, so is the $t_f = \Delta t_{DES} + \Delta t_{DATA} + \Delta t_{ASC}$. After touching the seabed at the target depth, the lander samples data for Δt_{DATA} seconds, previously programmable by the timer $\Delta t_{timer} = \Delta t_{DATA} + t1$. By calculating vertical descent displacement (see Eq. A.25–A.31 in Appendices), since $\Delta t_{DES} = t_1 - 0 = t_1$, it is possible to obtain t_1 and t_2 (Eq. (A.33). The related derivation, is presented in Eq. A.32–A.34 of Appendices.

$$t_1 = \frac{m_{\mathrm{des}}}{k_{\mathrm{des}} v_{T_{\mathrm{des}}}} \cosh^{-1}\left(e^{\frac{k_{\mathrm{des}}}{m_{\mathrm{des}}} Z_{max}}\right) \tag{A.33}$$

$$t_2 = \Delta t_{DES} + \Delta t_{DATA}$$

2.3.6. Ocean currents

One approach in modelling ocean currents can be in computing the ocean current velocity (v_w) as a function of depth. Ocean current meters can obtain such information from the specific location and deployment time. However, since one study constraint was to streamline the apparatus to facilitate aquatic monitoring, this is not required, although it can be complementary to additional peripheral devices.

One approach may be to resort to satellite remote sensing. For depths <30 m of the upper ocean layer, a constant value for ocean current can be obtained from the NASA Earth Data public dataset: Ocean Surface Current Analyses Real-time (OSCAR) Surface Currents - Near Real Time 0.25 Degree (Version 2.0, Lagerloef et al., 1999). The OSCAR's

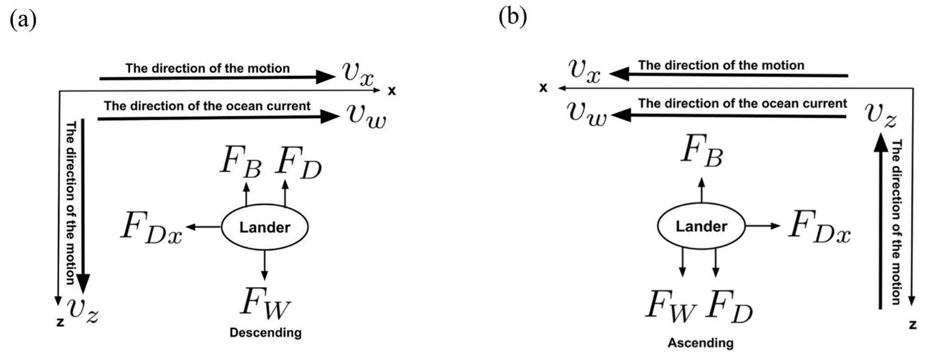

Fig. 5. Lander's model with fundamental forces (lander's weight F_W, drag force F_D, and buoyancy F_B forces) during descent (a) and ascent (b). Ocean medium and currents cause a drag force on the lander, making the lander instantaneously reach both the horizontal and vertical terminal velocities.

simplified ocean current model uses satellites for sea surface height gradients, encompassing ocean vector winds and sea surface temperature gradients. This is a simplified physical model for geostrophic, Ekman, and thermal wind dynamics (Roemmich, 1983). OSCAR does not include the tidal currents, and while they may be an important horizontal current component in estuaries, they are not modelled in this study, since the study location is a volcanic island with steep gradients. Section 4.1 presents the information about the quantitative estimate describing how barotropic tides would contribute solely to <7 drift in this test. The OSCAR dataset uses daily averaged surface currents, being provided on a global 25×25 km grid.

However, as OSCAR suffers from a low spatial resolution, it cannot resolve the sub-grid dynamics which are relevant in this study. This sea current dynamics is induced by the wind motion near the sea surface, causing Ekman transport (Ekman, 1905; Vallis, 2017) to occur in the surface layer. Instead of using the grid averaged OSCAR data for velocity and heading of the surface layer, the real-time on-board sonar sensing was used (see Fig. B.4) in Ekman's solution for the exponential decay of velocity with depth: $u,v \sim e^{-z/D_E}$, where u and v are zonal and meridional ocean current velocity components, z is the depth, and D_E is the characteristic width of Ekman layer. This direct approach allows us to smoothly connect the surface layer velocity profile with the empirical profile of ocean currents at greater depths.

For the day of deployment (March 11, 2024), the sonar readings were used to set the upper boundary for the surface layer horizontal velocity magnitude and direction for depths <90 m. For depths >90 m, given the unavailability of the datasets and costly transducers, this study relied on the shipborne 38 kHz Acoustic Doppler Current Profiler (ADCP) profile collected nearby on 02 March 2024 (Kopte et al., 2024) during MSM126 (32.60358° N, −16.88877° W), i.e., 9 days earlier and ≈3.9 km from the drop site, within the same OSCAR quadrant. Obtained ocean current depth profile spanned epipelagic and mesopelagic zones (from 38 to 1302 m, seen in Fig. 6).

To couple the two datasets, a depth-dependent ocean current is defined piecewise: Ekman exponential decay for $z \leq 90$ m, and spline fit to the ADCP magnitudes for $z > 90$ m (Fig. 7). We carefully blend Ekman exponential delay with ADCP profile by choosing the optimal value for the Ekman depth coefficient $D_E = 90$ m which agrees with the typical quantities (Mellor, 1996), and which preserves continuity without affecting the integrated drift. This provides a simple, robust C0 match at the interface and numerically stable trajectories.

Probability Density Functions (PDFs) of ocean current magnitudes (or speed of water $v_w = \sqrt{u^2 + v^2}$) per depth bin (Fig. 6a) indicate mild ocean currents (less than 0.2 m/s) and follow the Maxwellian distribution. This is because they are the squared sums of both the u (zonal) and v (meridional) ocean current components, respectively, which individually follow the Gaussian distribution. Differences in magnitudes per depth also indicate mild variation up to 0.1 m/s (Fig. 6b). The computed PDFs of ocean current headings (or direction of water $\theta_w = atan(u/v)$) for each depth bin (Fig. 6c) indicate a weak bimodal distribution with two peaks at the depth range ∼ 0–200 m, with the former being the dominant heading of ∼100° and the latter with a heading of −100°. This clearly indicates a presence of the vorticity in the surface layer which is attributed to the mixing of surface and deep ocean currents. The motion at the depths greater than 200 m confirms the existence of the ocean current unrelated to the Ekman dynamics which is restricted to the surface layer. The vortices in the layer 0–200 m are most likely to cause a small net velocity which represents an average value in the observed quadrant in OSCAR data. Even though the averaged velocity vector in the OSCAR data is negligible, it still implies a slow drift in the direction of the deep ocean current in ADCP profiles. The differences in headings per depth in ADCP profiles (Kopte et al., 2024) indicate the maximum variation of headings between −20° and +20° (Fig. 6d) which are further used in numerical model.

2.3.7. *Horizontal velocity*

The model of horizontal velocity assumes the Ekman transport exponential decay for the depths until 90 m (Vallis, 2017). For depths up to 900 m, average ocean current magnitudes v_w for the whole ADCP depth data were obtained, with a 5th order spline polynomial interpolation as the best fit (Fig. 7). Since the fit does not provide realistic values for depths greater than 900 m due to errors in readings from the ADCP, such currents are modelled with a steady exponential function which asymptotically approaches the value of 0.07 m/s. This horizontal component of current velocity is further placed into the differential equation (A.40), where the horizontal drag force and ocean current v_w are used to obtain the lander's horizontal velocity component v_x (derivation presented in Eq. A.35–A.40 in Appendices).

$$\frac{dv_x}{dt} = \beta(v_w - v_x)^2, \beta = \frac{\mu A \rho_w}{2m} \tag{A.40}$$

The analytical solution requires a priori knowledge of the ocean's current depth profiles. However, in the absence of such datasets, the solution to this nonlinear differential equation (also known as the Riccati equation) cannot be determined analytically and needs to be determined using numerical methods such as the fourth-order Runge-Kutta method, adaptive step-size embedded fifth-order RK, Bulirsch-Stoer (BS), or others (Bini et al., 2011).

2.3.8. *Horizontal displacement*

As the model's X axis is collinear with the ocean current direction, from the lander's horizontal velocity component v_x, the lander's horizontal drift or radial excursion $x(z(t))$ is obtained relative to the drop point. Such estimates the landing point within a probability region (circular uncertainty areas depicted in Graphical Abstract), whose mean radius is the most probable value of the lander drifts along the X and Y axes. The same procedure is required to compute the radial excursion during the ascent. These calculations are performed using random walk

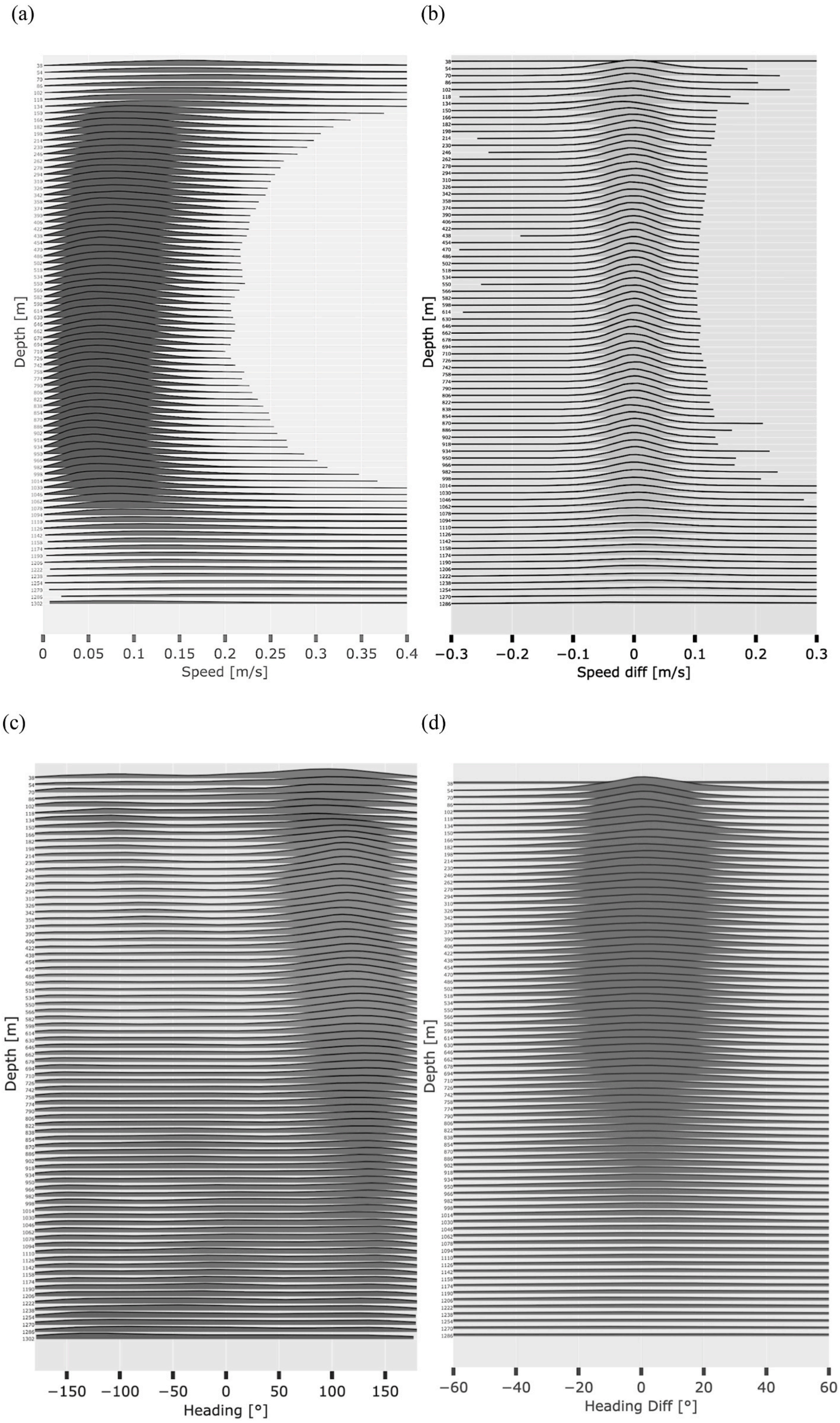

Fig. 6. Probability Density Functions (PDFs) of sampled ocean currents: (a) magnitudes, (b) magnitude differences, (c) phase angle headings, and (d) phase angle differences. PDFs are computed from a dataset obtained from shipborne ADCP (Kopte et al., 2024) during 02/03/2024 per depth bin of 16 m from 38 to 1302 m. Probability Density Functions (PDFs) of sampled ocean currents: (a) magnitudes, (b) magnitude differences, (c) phase angle headings, and (d) phase angle differences. PDFs are computed from a dataset obtained from shipborne ADCP (Kopte et al., 2024) during 02/03/2024 per depth bin of 16 m from 38 to 1302 m. Depths greater than 900 m indicate reading errors from the ADCP instrument.

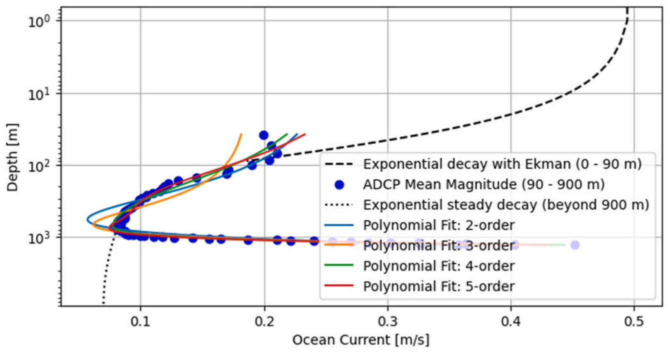

Fig. 7. Mean ocean current magnitudes (blue points) sampled from the ADCP survey on 02 March 2024 as a function of depth on a log scale. Spline interpolations are shown for different x-orders: two, three, four, and five polynomial orders. The top black line until 90 m depth is an exponential decay fit of Ekman transport, while the bottom black line beyond 900 m depth is an exponentially steady fit, avoiding the ADCP errors (Fig. 6). (For interpretation of the references to color in this figure legend, the reader is referred to the Web version of this article.)

numerical simulations.

3. Assessment

3.1. Numerical simulations

With an overall aim to facilitate subsurface ocean observations by creation of low-cost, easy-to-deploy deep-sea untethered small-sized landers, their deployment, sampling, and to probe the model based on fundamental physics and dead reckoning, it is essential to understand diverse ranges of outcomes and most likely scenarios during both the lander's descent and ascent dives. For that purpose, a random walk numerical simulation with 10^3 runs was used, respecting the computed terminal velocities during descent (1.4 m/s) and ascent (1.25 m/s) from individual physical components and characteristics (Fig. 4). The simulations are based on the physical model described in the previous section, that uses the solution of the Ekman transport equation with the boundary condition set to the readings (speed-over-ground (SOG) of $1\text{knot} \cong 0.5$ m/s) from the sea vessel sonar (see B.4), which is smoothly connected to the empirical dependencies from ADCP data. To populate the phase space with possible lander trajectories (Fig. 8), variations of the ocean current headings between -20° and $+20^\circ$ were included as obtained from ADCP data. Such a range was consistent with the obtained standard deviations of heading differences per depth bin from ADCP readings (Fig. 6d). Headings were further sampled following a Gaussian distribution with a mean of 0° and a standard deviation of 20°.

Fig. 8 shows the results of our numerical simulations calculating the lander's drop, landing and pop points as well as its underwater trajectories at the depths of 90 m (Fig. 8a, b, 8c), 900 m (Fig. 8d, e, 8f), and 9000 m (8g, 8h, 8i), respectively. When simulating the real deployment at 90 m depth, the lander's mean radial excursion (drop to landing to pop displacement along the X axis) was ~37 m with a maximum heading uncertainty of 33° (along the Y axis) and excursion time of 138 s (2.3 min), excluding the sampling time at the seabed. Additional simulations were performed at 900 m depth, where the lander's mean radial excursion was 137 m with a maximum heading uncertainty of 47° and 1364 s (~22 min) of excursion time. Also, observing the simulations at 9000 m, the lander's mean radial excursion was 863 m with a maximum heading uncertainty of 89° and 13,630 min (~3.8 h) of excursion time.

3.2. Field deployment

The lander's numerical simulations for depth of 90 m were used in the previous section to model a single deployment (Fig. 2) which was carried out on March 11, 2024, in the pelagic zone 1 km south of Funchal (see dive log in Table B3 of Appendices), Madeira Island, NE Atlantic. The deployment location was inside the same OSCAR quadrant with a centroid of 32.50° latitude and -16.75° longitude (Fig. 9). The deployment included the benthic lander with baits (Fig. 2). The used sea vessel was a 10 m semi-rigid sea vessel carrying GNSS and sonar instrumentation from the Ocean Observatory of Madeira (OOM). The maximum depth was obtained (Z_{max}, 90 m) from the sea vessel's sonar (see Sonar Readings in Figure B4 in Appendices), selected by the marine ecologists. The landing point depth at the seabed was assumed to be the same depth as the drop point. See Figure B4 in the Appendices for the bathymetry during deployment. The ADCP transect used (MSM126 on 02/03/2024) was ~3.9 km from the drop site and within the same OSCAR quadrant.

Since the lander has several buoys and is relatively lightweight without ballast (8.4 kg), the surface wind may also cause drift of the lander and impact the georeferencing trajectory (Wagner et al., 2022). For this reason, the magnitude and direction of both the ocean and wind currents were derived from their available u and v components. Ocean current data were taken from OSCAR[3] (Dohan, 2017) and wind data from ERA5[4] (Hersbach et al., 2020) datasets, both taken as a daily average. Both datasets are depicted in Fig. 9 during the deployment date at 12:00 UTC. The average magnitude of the total ocean current $v_w = \sqrt{u^2 + v^2}$ at the deployment area was 0.03 m/s with an average direction $\theta_w = (atan\,2(u,v) \times 180/\pi + 180) \mod 360$ of 347.22°. The wind speed was 4.19 m/s with the azimuth of 107.41°.

As the wind data has a sparse granularity, information from the official wind station at Madeira International Airport, located on the south coast of Madeira Island (approximately 200 m from the sea), was retrieved through Iowa State University's Iowa Environmental Mesonet (IEM), which maintains a global record of Meteorological Aerodrome Reports (METAR). Positioned close to the coastline (triangle in Fig. 9), the airport's location captures local orographic effects that influence wind direction, offering a more representative value for the wind conditions at the drop point. In the METAR report (LPMA 111200Z 05006 KT 010V080 9999 SCT015 19/09 Q1024), the official 10-min mean wind speed was recorded as 3.1 m/s with the azimuth of 50°, and it is illustrated in Fig. 9. Fig. 12a shows the average surface wind speed (ERA5 and METAR) of 3.20 m/s with the heading of 263.45°.

An additional custom logger (Radeta et al., 2024) was attached to the benthic lander to obtain the timestamp, depth, temperature, and drop and pop points' latitude and longitude, all sampled at 1 Hz. The drop point water temperature was 20.7 °C, while the landing point water temperature was 17.8 °C at a depth of 90 m.

3.2.1. Baseline terminal velocities

From the obtained depth and timestamps, empirical vertical terminal velocities were obtained (Fig. 10). The same figure also shows the modelled terminal velocities based on physical characteristics (Figs. 3 and 4). At the drop point and moment t_0, both the descent and ascent terminal velocities were reached within the first 3 s, after which the lander's velocities reached the plateau. The descent terminal velocity (average speed computed from logger readings) was 1.216 m/s, while the ascent was 1.125 m/s (Fig. 10b). This is consistent with the literature (Giddens et al., 2021) and provides controlled speed. Minor oscillations in terminal velocity readings from the logger indicate the presence of the vertical shear. Descent dive time (obtained from the logger) to the

---

[3] Ocean current dataset: Ocean Surface Current Analyses Real-time (OSCAR) Surface Currents - Interim 0.25 Degree (Version 2.0). Ver. 2.0. PO.DAAC, CA, USA. Accessed [2024-03-20] at https://doi.org/10.5067/OSCAR-25I20.

[4] Wind dataset: Copernicus Climate Change Service, Climate Data Store (2023): ERA5 hourly data on single levels from 1940 to present. Copernicus Climate Change Service (C3S) Climate Data Store (CDS). Accessed [2024-03-20] at https://doi.org/10.24381/cds.adbb2d47.

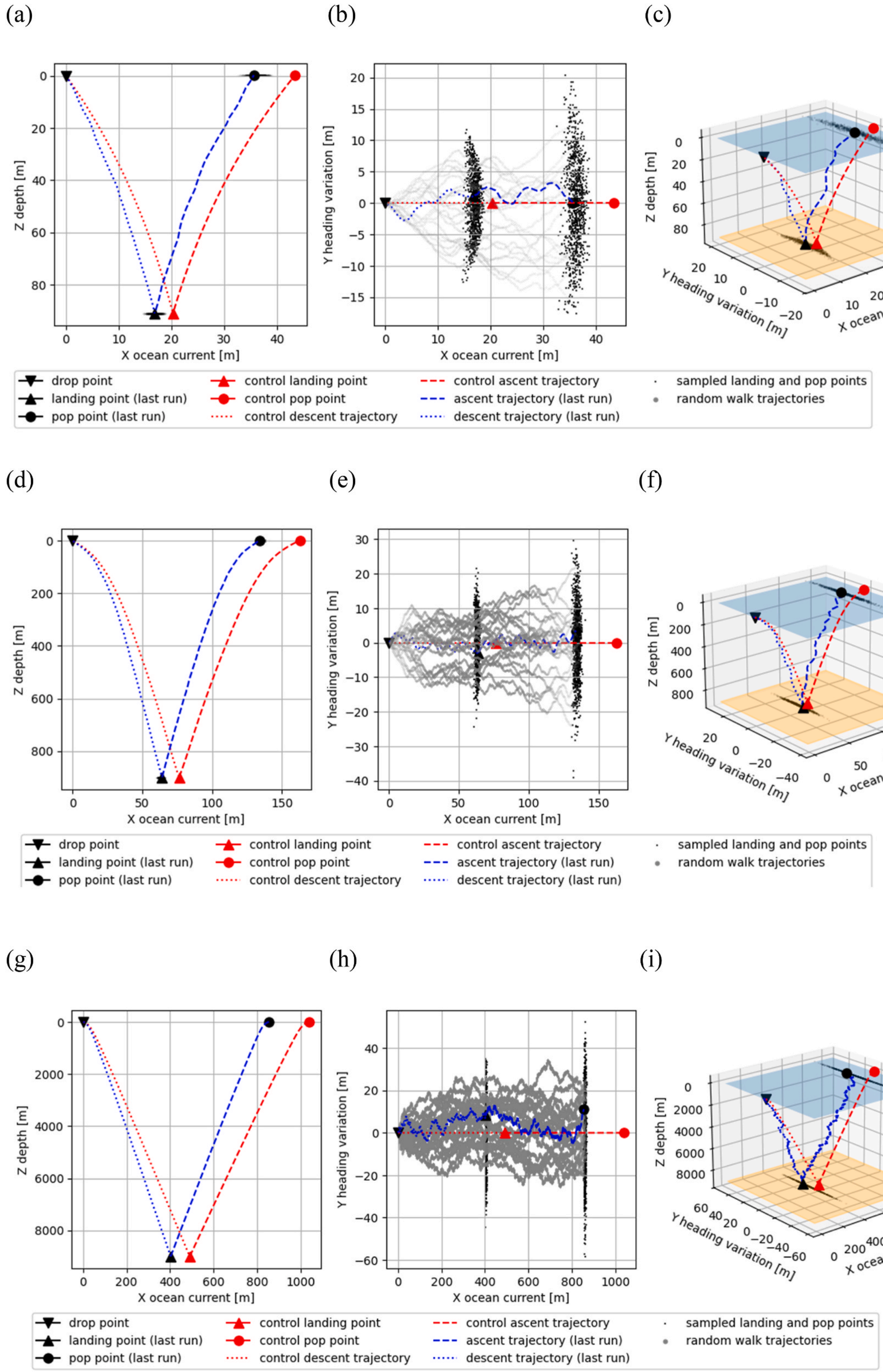

Fig. 8. Numerical simulation random walk results after 10^3 runs depicting lander trajectories during descent and ascent for depths: (a, b, c) 90 m, using exponential decay of Ekman transport; (d, e, f) 900 m, using combined exponential decay and ADCP control polynomial spline fit. Red line - control polynomial spline fit with 5° (Fig. 7). Blue line - last run from random walk simulation with heading variations between −20° and +20°. Blue area: sea surface. Orange area - seabed. Numerical simulation random walk results after 10^3 runs depicting lander trajectories during descent and ascent for depth of 9000 m, using a steady exponential decay function. Red line - control polynomial spline fit with 5° (Fig. 7). (For interpretation of the references to color in this figure legend, the reader is referred to the Web version of this article.)

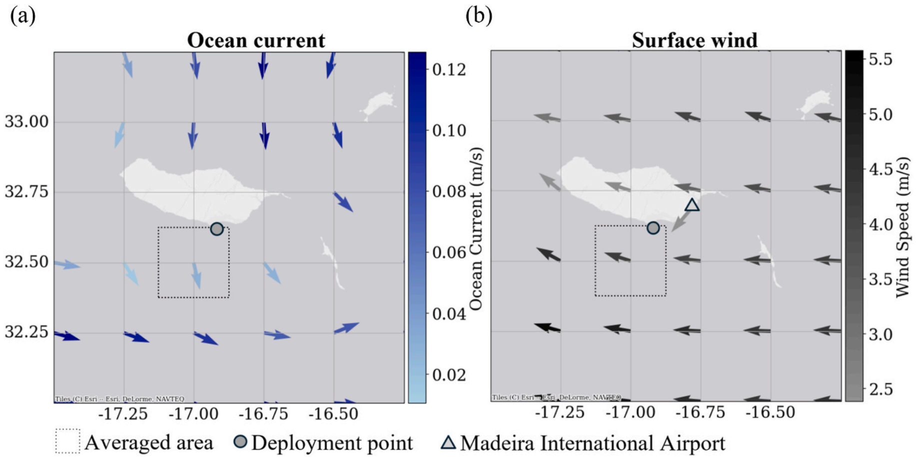

Fig. 9. Ocean current (daily average) and wind speed (daily and 10-min average) magnitude and heading during the deployment day on 11/03/2024 at 12:00 UTC.

landing point (t_1) was 75 s, while the ascent dive time to the pop point (t_f) took 80 s, indicating a longer ascent dive time by 5 s. This is due to the lander's differences in weight and buoyancy between descent (26.8 kg, including the ballast) and ascent (8.4 kg, excluding the ballast). Because the lander spends only ≈25 s descending and ≈27 s ascending through the upper 30 m (empirical terminal speeds ≈1.216 and 1.125 m/s), the OSCAR surface current (0.03 m/s on 11/03/2024) contributes ≈1.5 m horizontal drift in total; even assuming 0.10 m/s, the contribution would be ~ 5 m. This is small relative to the observed ≈27–30 m excursion driven by the 30–90 m shear resolved by the ADCP, which required a more thorough analysis using the Ekman transport.

3.2.2. *Estimated terminal velocities*

For the descent, the terminal velocity calculated from the model was 1.4 m/s. The experimental data indicate a slightly lower velocity, averaging around 1.2 m/s with minor fluctuations. Pearson's R correlation coefficient between the experimental and modelled velocities is 0.986, and a p-value of 0.0294 confirms the statistical significance of this correlation at the 5% significance level, indicating that the observed linear relationship is unlikely to be due to chance. Slight discrepancies may stem from factors such as measurement errors or drag force caused by the individual component areas. For the ascent, the terminal velocity predicted by the model was 1.25 m/s, while the experimental data approached tangentially, reaching approximately 1.2 m/s in about 3 s. In this case, Pearson's R correlation coefficient was 0.8594 with a p-value of 0.0283, also confirming the significance of positive correlation at the 5% significance level. As in the case of the descent, this demonstrates a good agreement between the experimental and modelled velocities, supporting the model's reliability.

3.2.3. *Predicted pop point*

From the onboard logger, the untethered lander's drop and pop points were obtained and depicted in Figs. 11a and b in green and red colors, respectively. A detailed log of the deployment is shown in Table B3 inside the Appendices. The obtained Euclidean distance between the drop and pop points was 27 m (Fig. 11c). Since this encompasses both the descent and ascent radial excursions, this agrees with the numerical simulations (Fig. 11d), which estimate the radial excursion to and from a depth of 90 m to be 38 m. This suggests the model had an error of ~40% in predicting the lander's pop point.

The lander's horizontal heading and drift were also verified empirically using the sea vessel sonar during the descent by switching off the engine and allowing the sea vessel to align with the sea currents, obtaining 263° current over ground (COG) during the deployment (see Figure B4 in Appendices). Figure B4 shows the dominant linear behaviour of the drift for the upper water column until 90 m, which is in line with the heading obtained using numerical simulations (Fig. 8). Fig. 12 shows that the computed bearing between drop point (32.62922, −16.91667) and pop point (32.62913, −16.91694) was 248.41° which is similar to the measured COG value of 263° at the ocean surface. Also, the wind at the airport (METAR) is aligned with the coastline due to orographic influences, like flow splitting and mountain waves (Belo-Pereira and Santos, 2021), and considering that the test was conducted in Funchal, where wind conditions from ERA5 can differ substantially from those at the airport due to local topographic effects, it is appropriate to use the average between ERA5 and METAR data as a first-order fusion approach (Fig. 12a).

This averaging acts as a simple blending technique, analogous to the methodology proposed by prior work (Escobar and Alvarez, 2023), who demonstrated that combining reanalysis and in situ or remotely sensed datasets can significantly reduce local inaccuracies in wind field estimation. The resulting average wind heading (248.41°) aligns with the bearing between the drop and pop points and shows an uncertainty of 15.04°, consistent with the expected variability of about 20°.

3.3. *Case full ocean depth*

In addition to the performed field study, the scenario for full ocean depth has also been computed numerically. Since the obtained ADCP sea current profiles have errors above 900 m (Fig. 7), for depths beyond the 900 m to full-ocean-depth, the steady current velocity with the value of 0.07 m/s has been assumed as it asymptotically approaches that value in ADCP survey (Kopte et al., 2024). Additional numerical simulations were performed with 10^3 runs with the case study at 9, 90, 900, 1,000, 3, 000, 5,000, 7,000, 9000 and 11,000 m with the same descent (1.4 m/s) and ascent (1.25 m/s) terminal velocities. The mean time (minutes), mean radial excursion (m), and heading uncertainties (m) are shown in Fig. 13. With an order of magnitude of depth, there is an exponential increase in the dive time as well as in the radial excursion (the displacement along the X-axis).

In the case of full-ocean-depth (11,000 m), the grand average obtained radial excursion for both the descent and ascent is ~1038 m, with heading uncertainty of 95° and the grand average dive time is 278 min (4.6 h), consistent with the literature (Bagley et al., 2004). Assuming the variable ocean current headings (−20° to +20°), the tendency of the heading uncertainty (displacement error along the Y axis) is nearly linear with the increase of magnitude (yellow bars in Fig. 13). This implies that the recapture of the equipment from the deepest ocean depths needs to be performed within a perimeter of 50 m relative to the centroid of the estimated pop point.

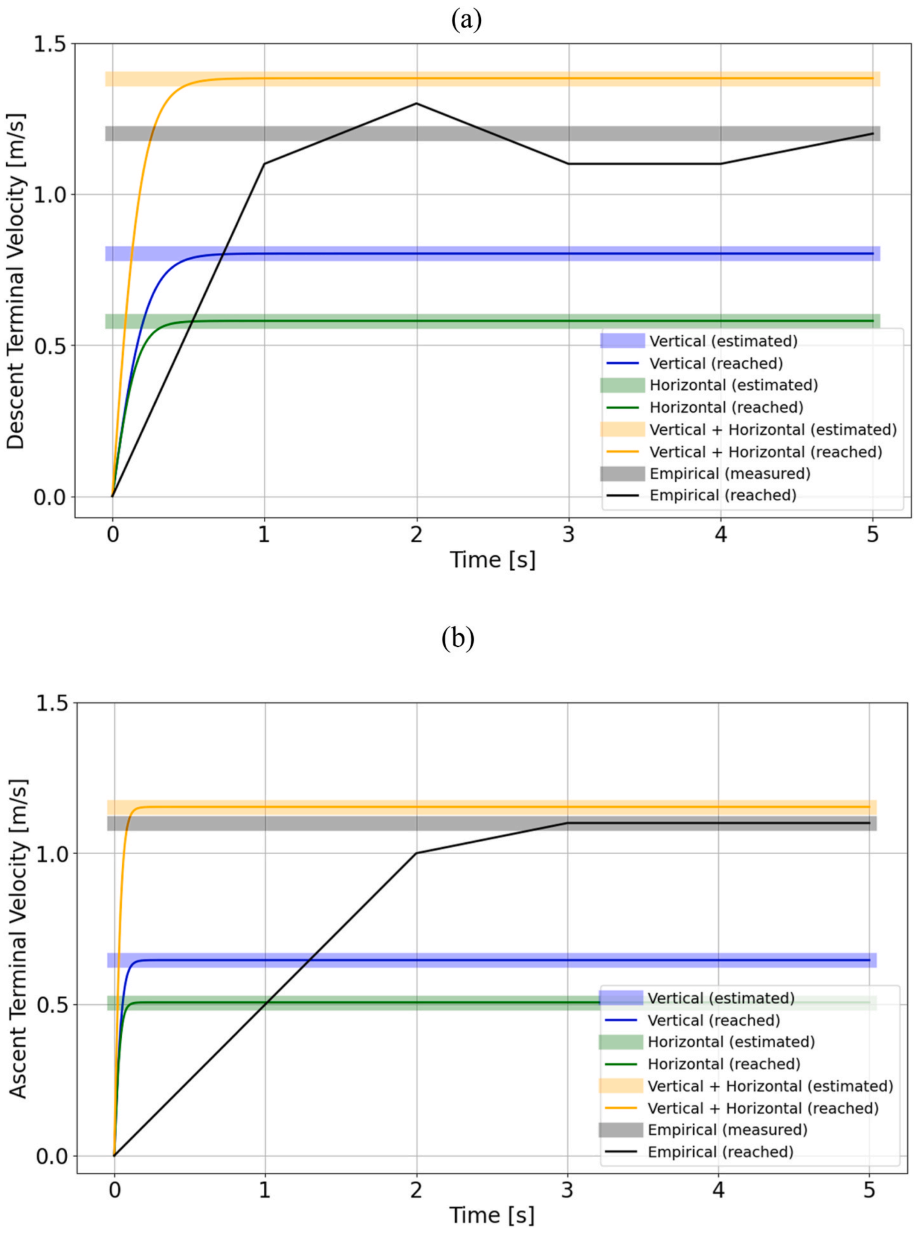

Fig. 10. Benthic lander's speed (terminal velocities) during descent (a) and ascent (b) from drop and to pop points. Black curve: empirical data; Colored curves: model calculated from Figs. 3 and 4. Both descending and ascending speeds converge to modelled terminal velocities (plateau at appx 1.2 m/s, consistent with Giddens et al., 2021).

4. Discussion

A novel georeferencing method is presented for low-cost untethered landers based on fundamental physics, facilitating the deployment and recapture of the subsurface ocean observatories. The study focused on predicting the untethered lander's landing and pop points at the seabed and sea surface, respectively, in an effort to allow more deployment, sampling, and successful recapture of the affordable Eulerian observatories. The model used the physical characteristics of the lander to model the buoyancy, drag, and weight forces, including the drift caused by ocean and wind currents. The ocean currents were modelled using an analytic solution of the Ekman transport (Vallis, 2017) for the depths 0–90 m, and ADCP surveys for the depths beyond 90 m. The model does not take into account other types of forces that may be involved in the system, such as those of tension on the used lines (Huang et al., 2007) or the tidal forces (Garrett and Maas, 1993). This work focused on paving the way towards more accessible Eulerian observatories, providing more affordable means for their use. The method proposed here may not be used only to simplify the existing complex and costly techniques in georeferencing such equipment at the sea bed and at the sea surface (Yu et al., 2022) but also to increase their recapture rate and ultimately reduce the potential hazards to the seabed, pipelines, or surface infrastructure (Kawsar et al., 2015) as an alternative to complex robotics (Liljebäck and Mills, 2017).

4.1. Modelling versus field deployment

When modelling the ocean currents, one can argue that the tidal currents should be part of the model and are very important in limited continental shelf regions, which include bays and estuaries (Clarke and Battisti, 1981), and thus should be included. However, in this study, the tidal currents were not considered as primary, as the focus of the study is on providing more subsurface observations, which, although it implies having less precision, also provides more access to deep-sea and open

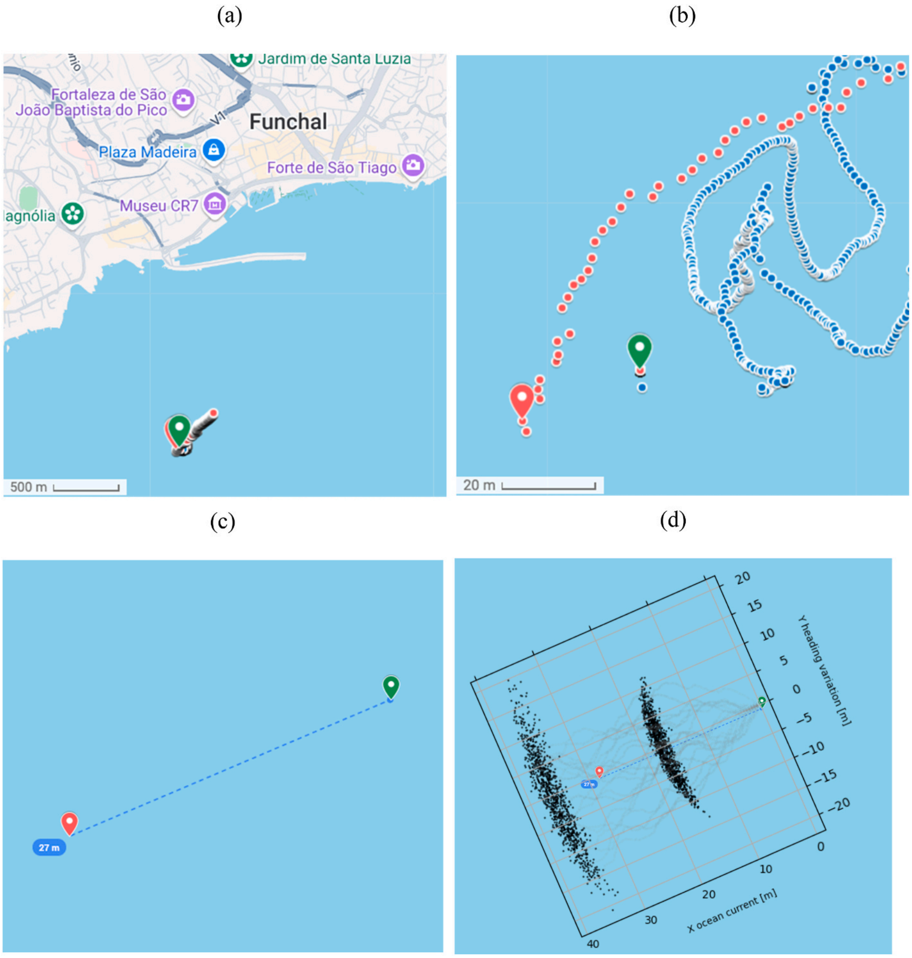

Fig. 11. Untethered lander deployment drop at latitude, longitude = 32.62922, −16.91667 (green pin) and pop points at 32.62913, −16.91694 (red pin) at 12:00 and 13:01:27 UTC, respectively, south of Funchal in Madeira island, NE Atlantic. Blue and red points indicate surface GNSS coordinates during the deployment and after recapture. (For interpretation of the references to color in this figure legend, the reader is referred to the Web version of this article.)

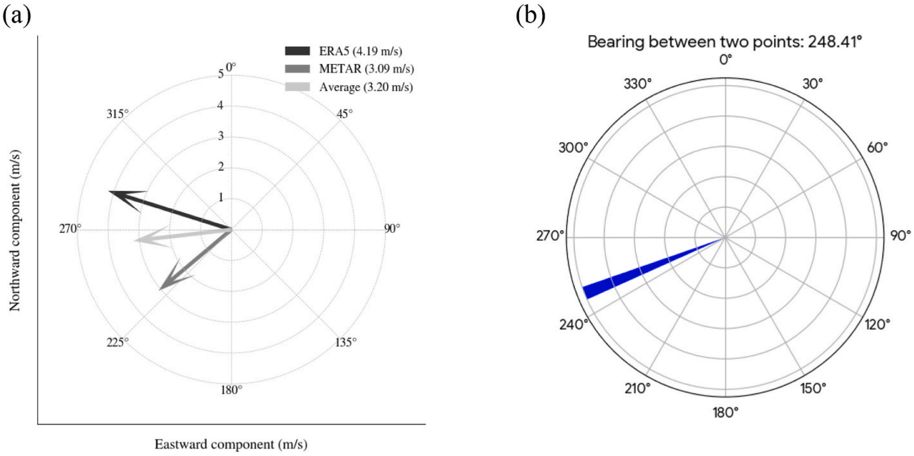

Fig. 12. (a) Wind average from Fig. 9; (b) computed drop/pop bearing from Fig. 11.

oceans deployments where other factors such as wind-driven currents and larger-scale oceanographic features are more dominant (Röhrs et al., 2023). While the single 90 m deployment was indeed carried out within the continental shelf (photic zone), the next considerations suggest excluding the tidal currents from the proposed main model (the model of the study based on fundamental physics is depicted in Section 2.2). First, the local barotropic signal was quantified, where the TPXO10-atlas solution (Egbert and Erofeeva, 2002) gave an M_2 depth-mean amplitude of 0.04–0.05 m/s for the tidal current at 32.64° N, 16.89° W (within the quadrant of the field deployment). Second, the 38 kHz ADCP transect within the quadrant of the field deployment (Kopte et al., 2024) measured 0.12–0.20 m/s between 30 m and 90 m—the layer that dominated the 155 s dive time (descent–ascent) of the untethered lander used in this study. Even if a coherent 0.05 m/s tide

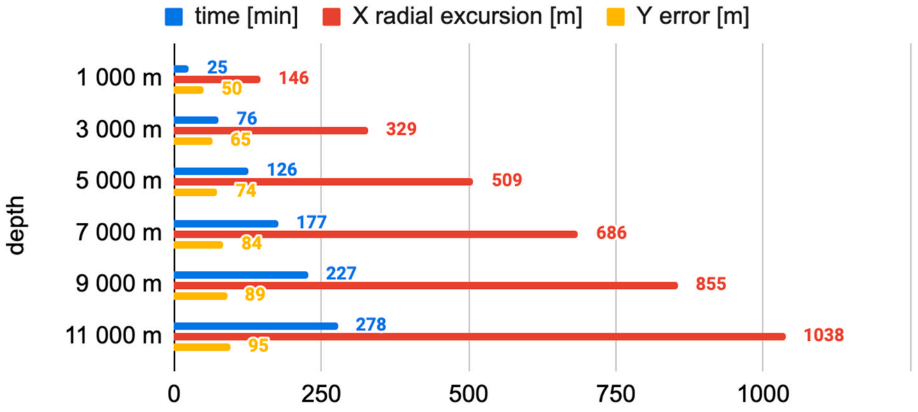

Fig. 13. Numerical simulations with 10^3 runs with mean average time, mean radial excursion, and mean heading uncertainty within 3 sigma.

persisted throughout that interval, the maximum extra drift would be < 7 m. The proposed model already reproduced the pop point to within 3 m of uncertainty, so any residual tidal contribution may lie within the present error envelope. While this rationale is adequate for the short, single-cycle test reported here, the authors of the study fully acknowledge that tidal forcing becomes increasingly important for multi-hour missions, for spring-tide conditions, and for shelf or channel sites where barotropic amplitudes can exceed 0.5 m/s.

Another important note of the field deployment it was decided to limit to the epipelagic (photic) zone with two rationales: (i) first, the untethered monitoring system considered in this study was the benthic lander, which was based on BRUVS. As such, the system contained the camera without any external lights, and any obtained footage would not be visible if carried out in the deep sea; (ii) second, most of the important biological processes and ocean current dynamics appear in the upper water column. After 200 m of depth, the ocean currents decrease in magnitude, and as such, they can be approximated as being constant (Tuchen et al., 2022).

4.2. Comparisons against the literature

Contrary to complex and costly untethered lander setups (Hardy and Kontoes, 2019), this study provides a location estimation focusing on affordable and custom-made aquatic monitoring systems, such as low-cost landers or BRUVs based on primer ignition auto-release mechanisms using natural cobble (Radeta et al., 2025), allowing their surface recapture. The proposed model also expands upon the prior work (Schmid, 1969) by enhancing it further with ocean current depth profiles and by calculating the radial excursion along both the X and Y axes using random walk numerical simulations with 10^3 runs. Moreover, it expands prior studies on free-falling descent analysis (Zhang et al., 2023) by incorporating horizontal drift, which has been neglected in the study performed by the authors due to the large lander's weight (above 600 kg). It also expands the analysis beyond controlled environments (such as in tanks or swimming pools), providing initial steps for in-situ pelagic and deep-sea deployments (Yasseri, 2014; Chu et al., 2005). Also, it builds upon the existing standards for protecting underwater pipelines (Veritas, 2010) by providing initial insights into the possible trajectories of future, smaller-sized landers. Conversely, a reported study complements the existing efforts in calculating and optimizing the drag force coefficients of bodies penetrating the fluids, ultimately allowing the customization of the required horizontal and vertical terminal velocities and controlled descent of vehicles with buoyancy engines (Yin et al., 2024).

4.3. Study limitations and future work

The robustness of the proposed method has several constraints. Although the Ekman transport is a known phenomenon, it is not sure how the wind driven Ekman rotation of the ocean current couples with the currents that originate at greater depths. Also, subtidal currents in this study are neglected since the deployment was very near the south coast where local winds and waves are reduced. However they should be taken into consideration when modelling the ocean currents as they may vary on the weekly basis (Tai et al., 2017). For instance, currents around Madeira Island do show significant variability on weekly to multi-week timescales (Alves et al., 2023). However, deployment in this study was conducted during the spring when currents tend to be weaker, ranging from roughly 0.1–0.5 m/s (Alves et al., 2023). Furthermore, the vorticity observed in the layer closer to the surface (0–200 m) in the ADCP data implies the existence of complex structures which may lead to different results. Also, all carried out numerical simulations assume a constant value for depths beyond 1000 m (0.07 m/s).

All depths within the range of 90–900 m assume historical ADCP samples of ocean currents from the nearby transects in the region (Kopte et al., 2024). This means that although the near-real-time satellite telemetry may be accessible for the given hour of the deployment, for greater precision (and thus less fuel cost in search and recapture), it may require past knowledge of ocean currents from nearby ADCP surveys. Conversely, if ADCP datasets are from different latitudes, the ocean current depth profiles will naturally vary (Tuchen et al., 2022). Nevertheless, should the ocean current magnitude and heading be unknown from external datasets, the ocean current headings can be approximated using the sea vessel's compass.

In the case of hardware probes, contrary to the complex ADCP setups, the magnitude can be obtained with low-cost rotors (Wijaya, 2018) or vector measuring current meters (Way et al., 1996). These probes can be integrated within the proposed model. Also, the carried-out deployment process did not rely on the model to retrieve the lander, and it used the experienced skippers on board, focusing on scouting the sea surface for larger yellow fluorescent buoys.

Another important limitation is that all of the reported calculations dealing with predicting the landing and pop points were performed a posteriori, where a priori simulations are needed. This brings some possible pragmatic considerations during the deployment. For instance, during the deployment, an onboard computer with access to the internet is required to run the algorithm for predicting the landing and pop points based on real-time data. The proposed technique should be rigorously assessed in terms of practicality, starting from the experiment design, sampling currents/winds from remote sensing ad hoc on a sea vessel, running simulations to predict the landing and popping points, deploying the lander, returning to the harbour, and recapturing the lander, observing the results, and verifying/refining the results. All these can provide insights into assessing the recapture rates at different depths and at different sea states.

Also, the proposed model assumes that the depth at the drop point (obtainable from sonar, and used for analytical derivation) is the same as the actual landing point depth (see Graphical Abstract), which is an open issue. This implies that the technique may not be used with rapidly increasing slopes, as in the case of seamounts. Moreover, future georeferencing assessments should include the deployments beyond the equatorial shelf (epipelagic zone) and expand into the abyss.

With this work, our goal is to enable affordable, small-vessel deployments without acoustic or satellite telemetry. Real-time GPS or acoustic tracking increases mass, power, complexity, and cost, and can raise operational and environmental constraints, whereas our physics-based approach uses only lander geometry and open environmental datasets, yet achieved a 40% pop-point error at 90 m (Fig. 11). Remote sensing is used here to parameterize surface forcing; it cannot provide the submerged lander location itself. Where meter-level geolocation during multi-hour missions is critical, telemetry remains advisable; the present method targets low-cost operations where "tens of meters" bias materially reduces search time and fuel and is sufficient to georeference BRUVS-style observations.

CRediT authorship contribution statement

Marko Radeta: Writing – review & editing, Writing – original draft, Visualization, Validation, Supervision, Software, Resources, Project administration, Methodology, Investigation, Funding acquisition, Formal analysis, Data curation, Conceptualization. **Zahra Behboodi:** Writing – review & editing, Visualization, Validation, Software, Methodology, Formal analysis. **Vladimir Zekovic:** Writing – review & editing, Visualization, Validation, Software, Methodology, Investigation, Formal analysis. **Décio Alves:** Writing – review & editing, Visualization, Validation, Software, Methodology, Formal analysis, Data curation. **David Pestana:** Writing – review & editing, Visualization, Validation, Conceptualization. **Daniel Nunes:** Writing – review & editing, Visualization, Validation, Software, Data curation, Conceptualization. **Margarida Freitas:** Writing – review & editing, Visualization, Validation, Software, Data curation, Conceptualization. **Ankit Gupta:** Writing – review & editing, Validation, Methodology, Formal analysis, Conceptualization. **João Pestana:** Writing – review & editing, Validation, Data curation. **Dinarte Vieira:** Writing – review & editing, Visualization. **Sílvia Almeida:** Writing – review & editing. **Morgado Dias:** Writing – review & editing. **João Canning Clode:** Writing – review & editing, Resources, Funding acquisition. **Rui Caldeira:** Resources. **Paulo Relvas:** Writing – review & editing. **Antonio Vasiljevic:** Writing – review & editing.

Declaration of competing interest

Acknowledgments

This study was supported by the EU grants TWILIGHTED (Horizon EU Grant No. 101158714), CLIMAREST (Horizon EU Grant No. 101093865), SEAMPHONI (Horizon EU Grant No. 101206245) and by National Portuguese funding through projects INTERWHALE (FCT Grant No. PTDC/CCI-COM/0450/2020), Associate Laboratory MARE (FCT Grant No. UIDB/04292/2020), and Associate Laboratory ARNET (FCT Grant No. LA/P/0069/2020). JCC was funded by national funds through FCT- Fundação para a Ciência e a Tecnologia, IP, under the Scientific Employment Stimulus Institutional Call (CEECINST/00098/2018). SA was funded by the Foundation for Science and Technology (FCT) through the grant number UI/BD/151020/2021. AG was funded by the EU project LERCO (Grant No. CZ.10.03.01/00/22_003/0000003) via the Operational Programme Just Transition. VZ was financially supported by the Ministry of Education, Science and Technological Development of the Republic of Serbia through contract No. 451-03-136/2025-03/200104.

Appendices.

A. Theory and calculation

Below derivations encompass fundamental physics for modeling aquatic observation systems, including: (i) net forces, (ii) vertical terminal velocities, (iii) vertical velocities, (iv) vertical displacements, (v) dive time, (vi) horizontal velocities, and (vii) horizontal displacements.

A.1-A.4 Net Forces

From Newton's second law, the motion equation is:

$$F_{\text{net}} = ma \tag{A.1}$$

The force balance equation for descending (with positive z direction of motion) from the surface to the seabed is:

$$F_W - F_B - F_D = ma_z, \tag{A.2}$$

$$m_{des}g - \rho_w V_{des} g - k_{des} v_{des}^2 = ma_z$$

where fundamental forces acting on the lander are its weight F_W, drag F_D, and buoyancy F_B (Fig. 5). Lander has a mass *m (kg)* which during descent has an acceleration *g* (m/s^2) due to gravity. The ρ_w is the seawater density $\rho_w = 1023.6 kg/m^3$ at a temperature of 25 °C, salinity of 35 g/kg, and 1 atm pressure (Poisson et al., 1980). The V is the volume of displaced fluid equal to the lander's total volume, following Archimedes' principle. The v is the lander's velocity component along the movement direction.

For ascending (with negative z direction of motion) from the seabed to the surface is:

$$\begin{aligned} &F_W - F_B + F_D = ma_z, \\ &m_{asc}g - \rho_w V_{asc} g + k_{asc} v_{asc}^2 = ma_z, \end{aligned} \tag{A.3}$$

where k is the lander's constant, being one-half the product of the seawater density ρ_w that the lander displaces, the lander's frontal cross-sectional area pushing through the seawater A, and the lander's drag force coefficient μ, both changing during descent (A_{DES}, μ_{des}) and ascent (μ_{asc}, A_{ASC}):

$$\begin{aligned} k(\rho_w, A, \mu) &= \frac{1}{2}\rho_w A\mu \ \ (kg/m), \\ k_{des}(\rho_w, A, \mu) &= \frac{1}{2}\rho_w A_{des}\mu_{des}, \\ k_{asc}(\rho_w, A, \mu) &= \frac{1}{2}\rho_w A_{asc}\mu_{asc}. \end{aligned} \tag{A.4}$$

Since the coefficient μ varies with the material's shape (Heddleson et al., 1957), the A_{DES} is the sum of the cross-sectional area approximations of the: ballast as a circle; L-shaped BRUVs as a long cylinder; and spherical buoys as n circles, due to the group of n buoys. The same applies to the A_{ASC} being without ballast.

A.5-A.10 Terminal Velocity

Terminal velocity occurs when there is no acceleration ($a = 0$):

$$mg - \rho Vg - kv^2 = 0, \tag{A.5}$$

$$mg - \rho Vg = kv^2 \tag{A.6}$$

$$kv^2 = mg - \rho Vg, \tag{A.7}$$

$$v^2 = \frac{mg - \rho Vg}{k} \tag{A.8}$$

$$v_{T\,des} = \sqrt{\frac{m_{des}g - \rho_w V_{des}g}{k_{des}}}, \tag{A.9}$$

$$v_{T\,asc} = \sqrt{\frac{\rho_w V_{asc}g - m_{asc}g}{k_{asc}}}, \tag{A.10}$$

whose derivation is from (A.6), however, with $-k_{asc}v^2$ and the other ascending values.

A.11-A.24 Vertical Velocity

$$mg - \rho Vg - kv_z^2 = ma_y = m\frac{dv_z}{dt} \tag{A.11}$$

$$g - \frac{\rho Vg}{m} - \frac{k}{m}v_z^2 = \frac{dv_z}{dt} \tag{A.12}$$

$$-\frac{k}{m}v_z^2 + g - \frac{\rho Vg}{m} = \frac{dv_z}{dt} \tag{A.13}$$

$$-\frac{k}{m}\left(v_z^2 - \frac{mg}{k} + \frac{\rho Vg}{k}\right) = \frac{dv_z}{dt} \tag{A.14}$$

$$-\frac{k}{m}dt = \frac{dv_z}{\left(v_z^2 - \frac{mg}{k} + \frac{\rho Vg}{k}\right)} \tag{A.15}$$

Excluding the terminal velocity solution $\frac{dv}{dt} = 0 \Leftrightarrow v(t) = v_T$.

$$\beta^2 = \frac{mg - \rho Vg}{k} \tag{A.16}$$

$$-\frac{k}{m}dt = \frac{1}{v_z^2 - \beta^2}dv \tag{A.17}$$

$$-\int_0^t \frac{k}{m} \quad dt = \int_0^v \frac{1}{v_z^2 - \beta^2} \quad dv \tag{A.18}$$

$$\frac{k}{m}t\beta = \tanh^{-1}\left(\frac{v_z}{\beta}\right) \tag{A.19}$$

$$\beta = v_{T\,des} = \sqrt{\frac{m_{des}g - \rho_w V_{des}g}{k_{des}}} \tag{A.20}$$

$$\frac{v_z}{v_T} = \tanh\left(\frac{kv_T}{m}t\right) \tag{A.21}$$

$$v_{z\,des}(t) = v_{T\,des}\tanh\left(\frac{k_{des}v_{T\,des}}{m_{des}}t\right) \tag{A.22}$$

Similar methods may be used for ascending motion:

$$\beta = v_{T\,asc} = \sqrt{\frac{\rho_w V_{asc}g - m_{asc}g}{k_{asc}}} \tag{A.23}$$

Therefore, the solution for ascending velocity is:

$$v_{z\,asc}(t) = v_{T\,asc}\tanh\left[\frac{k_{asc}v_{T\,asc}}{m_{asc}}(t_2 - t)\right] \tag{A.24}$$

where t_2 is the time when ascending starts. This comes from (A.18), where the left integral now starts at t_2, not at 0. One can see that $v_{z\,asc}(t = t_2) = 0$, which is identical to $v_{z\,des}(t = 0) = 0$, confirming the physical intuitions.

A.25-A.31 Vertical Displacement

To find the position function $z(t)$, we integrate $v(t)$ from 0 to t:

$$z(t) = \int_0^t v_z(t) \quad dt = v_T \int_0^t \tanh\left(\frac{kv_T}{m}t\right) \quad dt \tag{A.25}$$

The indefinite integral of $\tanh(ax)$ with respect to x is:

$$\int \tanh(ax) \quad dx = \frac{1}{a}\ln(\cosh(ax)) + C \tag{A.26}$$

Applying this to the integral in A.25:

$$z(t) = v_T \int_0^t \tanh\left(\frac{kv_T}{m}t\right) \quad dt \tag{A.27}$$

this becomes:

$$z(t) = v_T \cdot \frac{m}{kv_T}\left[\ln\left(\cosh\left(\frac{kv_T}{m}t\right)\right)\right]_0^t \text{, or:} \tag{A.28}$$

$$z(t) = \frac{m}{k}\left[\ln\left(\cosh\left(\frac{kv_T}{m}t\right)\right) - \ln(\cosh(0))\right] \tag{A.29}$$

Since $cosh(0) = 1$ and $ln(1) = 0$, the expression simplifies to:

$$z_{des}(t) = \frac{m_{des}}{k_{des}}\ln\left[\cosh\left(\frac{k_{des}v_{T\,des}}{m_{des}}t\right)\right] \tag{A.30}$$

Integrating from Eq. (A.27), with ascending parameters, from t_2 to t:

$$z_{asc}(t) = -\frac{m_{asc}}{k_{asc}}\ln\left[\cosh\left(\frac{k_{asc}v_{T\,asc}}{m_{asc}}(t_2 - t)\right)\right] + Z_{max} \tag{A.31}$$

at $t = t_2$: $z_{asc}(t_2) = Z_{max}$, as expected.

A.32-A.34 Dive Time

Given that the $z_{des}(t)$ function reaches maximum value $Z_{\max}$ at the seabed, it is possible to calculate the descending time:

$$t_1 = t_{des}(Z_{max}) \tag{A.32}$$

Inverting Eq. (A.30) and evaluating it at $z = Z_{max}$, one can obtain:

$$t_1 = \frac{m_{\mathrm{des}}}{k_{\mathrm{des}}v_{T_{\mathrm{des}}}}\cosh^{-1}\left(e^{\frac{k_{\mathrm{des}}}{m_{\mathrm{des}}}Z_{max}}\right) \tag{A.33}$$

which is the time interval from the surface to the depth obtained a priori (read by the sea vessel's sonar).

Now the t_2 can be obtained (the moment when the ascent begins):

$$\begin{aligned} & t_2 = \Delta t_{DES} + \Delta t_{DATA} \\ \Leftrightarrow\; & t_2 = t_1 + \Delta t_{DATA} \\ \Leftrightarrow\; & t_2 = \Delta t_{timer} = t_{timer} \end{aligned} \tag{A.34}$$

remembering that Δt_{data} is the time at the seabed during sampling.

A.35-A.40 Horizontal Velocity

From Newton's Second Law, considering the only horizontal force present is a sideways hydrodynamic drag force, which is a function of the relative velocity between the object (v_x) and the ocean current (v_w). One can formulate mathematically as:

$$F_x = ma_x \Leftrightarrow f_x = m\frac{dv_x}{dt}, \tag{A.35}$$

$$\frac{\mu A \rho_w}{2}(v_w - v_x)^2 = m\frac{dv_x}{dt}, \tag{A.36}$$

$$\frac{dv_x}{dt} = \beta(v_w - v_x)^2, \beta = \frac{\mu A \rho_w}{2m}. \tag{A.37}$$

Due to the quadratic nature of the relative velocity term in A.37, it is necessary to explicitly separate the equation into the two possible scenarios.

$$\frac{dv_x}{dt} = \begin{cases} \beta(v_w - v_x)^2, v_x \le v_w \\ -\beta(v_w - v_x)^2, v_x > v_w \end{cases} = (-1)^{H(v_x - v_w)}\beta(v_w - v_x)^2, \tag{A.38}$$

where H is the Heaviside function, or:

$$H(v_x - v_w) = \{\, 0, v_x \le v_w 1, v_x > v_w\,. \tag{A.39}$$

Using shorthand notation becomes:

$$\left\{ \frac{dx}{dt} = v_x \frac{dv_x}{dt} = (-1)^{H(v_x - v_w)}\beta(v_w - v_x)^2 \right. . \tag{A.40}$$

A.41-A.42 Horizontal Displacement

Since the final goal is to obtain the trajectory $x(z)$, and given that the equation of motion in the vertical direction A40 has an explicit form, one can use the chain rule in the following to yield only one system of equations needed to compute the final path.

$$\left\{ \frac{dx}{dt} = \frac{dx}{dz}\frac{dz}{dt} = v_x \frac{dv_x}{dt} = \frac{dv_x}{dz}\frac{dz}{dt} = (-1)^{H(v_x - v_w)}\beta(v_w - v_x)^2 \right. \tag{A.41}$$

Given that $\frac{dz}{dt} \equiv v_z$, with a variable change $v_z(t(z)) = v_z(z)$, the set of equations can be written in the form:

$$\left\{ \frac{dx}{dz} = \frac{v_x}{v_z}\frac{dv_x}{dz} = (-1)^{H(v_x - v_w)}\frac{\beta}{v_z}(v_w - v_x)^2 \right. , v_z \ne 0. \tag{A.42}$$

B. Tables and Figures

B.1 Lander measurements

Table B1

Untethered benthic lander's measurements. Legend: d-Diameter [cm], L-Length [cm], A-Area [cm^2], w-Weight [g], V-Volume [cm^3], ρ-Density [g/cm^3], μ-Drag force coefficient [dimensionless], VRT-Vertical, HOR-Horizontal, IN-Inside, OUT-Outside, DES-Descent, ASC-Ascent. Bold values indicate the most significant component volumes that displace water.

(a)	(b)		(c)	(d)	(e)		(f)	(g)	(h)	
Unit	Qty.	Component	*d*	*L*	A		w	V	μ	
					VRT	HOR			VRT	HOR
Buoyancy	3	Small buoy	12.6	n/a	124.69	124.69	280	**967.5**	0.4	0.4
	1	Large buoy	18.0	n/a	254.47	254.47	883	**2952**	0.4	0.4
Payload	1	VRT support	2.09	80	3.43	167.2	199.5	142.5	1.15	0.963
	1	HOR Support	2.09	73.5	153.62	3.43	166.7	129.2	0.95	1.13
	1	Bait canister	7.5	26.5	540.9	33.17	301	**878.91**	1.35	0.82
	2	T-connection	1/2″ FFF		14.67	5.43	168.3	21.04	0.85	0.85
Timer	1	Timer	☐ 4 x 3.5		14	14	33.4	25.3	1.05	1.00
	2	Double swivel	0.8	8.71	9.02	6.97	153.38	19.54	0.74	0.82
Ballast	1	Natural cobble	18.15 x 12.15 x 6.58		700.8	247.11	17629	**6078,97**	0.74	0.4
			Total		A (VRT/HRT)		w	V	μ (VRT/HRT)	
			(i)	DES	700,8	1072,69	20696	**12812**	6,72	6,63
			(j)	ASC	389,28	825,57	3067	**6733**	6,35	6,43

B.2 Lander's coefficients

Table B2
Calculated lander's coefficients ready for deployment, including both the vertical and horizontal profiles, and including descent and ascent dives.

Lander's coefficient	Vertical profile (V)	Horizontal profile (H)	Sum (V + H)
k_{des}	115.39	221.16	336.55
k_{des}	88.74	144.53	223.27

B.3 Dive Log

Table B3
Benthic lander dive log obtained from the placed sensor on March 11, 2024, during deployment in the pelagic area of Madeira Island, NE Atlantic. The n/a indicates that the GPS sensor is being submerged in the water.

Epoch	Local time	Latitude	Longitude	Moment	Description
1710154801	11:00:01	32.629209	−16.916356	–	Lander was placed in water
1710154809	11:00:09	32.629229	−16.916679	t_0	Descend start (drop point)
1710154880	11:01:20	n/a	n/a	–	Image from sonar taken
1710154883	11:01:23	n/a	n/a	t_1	Touchdown (landing point)
1710158410	12:00:00	n/a	n/a	–	Primer ignition
1710158410	12:00:10	n/a	n/a	t_2	Ascend start
1710158489	12:01:29	n/a	n/a	t_f	Ascend end (pop point)
1710158647	12:04:07	32.62913	−16.916694	–	Lander recapture

B.4 Sonar Readings

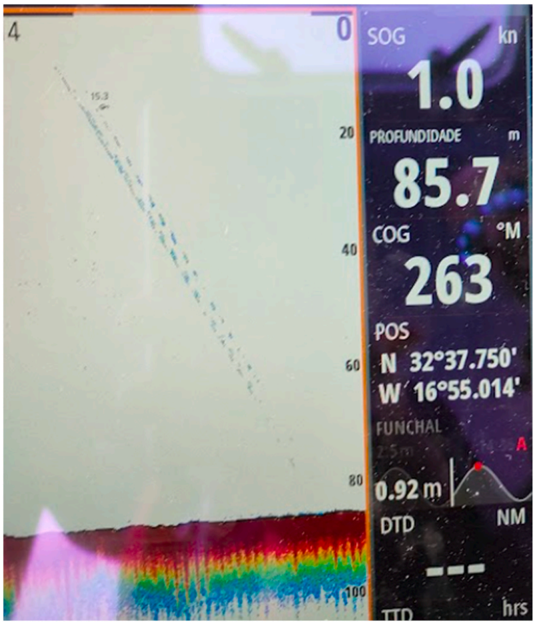

Fig. B4. Sonar readings from the sea vessel during benthic lander deployment in the pelagic area of Madeira Island, NE Atlantic, on March 11, 2024, at 11:01:20 GMT. The figure depicts the linear horizontal drift caused by the sea currents.

Data availability

Data will be made available on request.

References

Aanesland, V., 1987. Numerical and experimental investigation of accidently falling drilling pipes. In: Offshore Technology Conference. OTC. OTC-5497).

Afonso, M.M., 2008. The terminal velocity of sedimenting particles in a flowing fluid. J. Phys. Math. Theor. 41 (38), 385501.

Almeida, J., Soares, E., Almeida, C., Matias, B., Pereira, R., Sytnyk, D., et al., 2024. Robotic data recovery from seabed with optical high-bandwidth communication from a deep-sea lander. In: OCEANS 2024-Singapore. IEEE, pp. 1–7.

Alves, J.M., Miranda, P.M., Caldeira, R.M., 2023. Low-level jets drive the summer intra-seasonal variability of the Canary upwelling system. Front. Mar. Sci. 10, 1068134.

Ardhuin, F., Aksenov, Y., Benetazzo, A., Bertino, L., Brandt, P., Caubet, E., et al., 2018. Measuring currents, ice drift, and waves from space: the sea surface KInematics multiscale monitoring (SKIM) concept. Ocean Sci. 14 (3), 337–354.

Bagley, Philip Michael, et al., 2004. Lander techniques for deep-ocean biological research. Underw. Technol. 26 (1), 3–12.

Bell, D.R., Ledoit, O., Wolf, M., 2024. A novel estimator of Earth's curvature (Allowing for inference as well). Ann. Appl. Stat. 18 (1), 585–599.

Belo-Pereira, M., Santos, J., 2021. Air-traffic restrictions at the madeira international airport due to adverse winds: links to synoptic-scale patterns and Mountain wave phenomena. In: EGU General Assembly Conference Abstracts, pp. EGU21–6116.

Berkenpas, E.J., Henning, B.S., Shepard, C.M., Turchik, A.J., Robinson, C.J., Portner, E. J., et al., 2017. A buoyancy-controlled lagrangian camera platform for in situ imaging of marine organisms in midwater scattering layers. IEEE J. Ocean. Eng. 43 (3), 595–607.

Bini, Dario A., Iannazzo, Bruno, Meini, Beatrice, 2011. Numerical Solution of Algebraic Riccati Equations. Society for Industrial and Applied Mathematics.

Chu, P.C., Gilles, A., Fan, C., 2005. Experiment of falling cylinder through the water column. Exp. Therm. Fluid Sci. 29 (5), 555–568.

Clarke, A.J., Battisti, D.S., 1981. The effect of continental shelves on tides. Deep-Sea Res., Part A 28 (7), 665–682.

Cristini, L., Lampitt, R.S., Cardin, V., Delory, E., Haugan, P., O'Neill, N., et al., 2016. Cost and value of multidisciplinary fixed-point ocean observatories. Mar. Pol. 71, 138–146.

Dohan, K., 2017. Ocean surface currents from satellite data. J. Geophys. Res., Oceans 122 (4), 2647–2651.

Dominguez-Carrió, Carlos, Fontes, Jorge, Morato, Telmo, 2021. A cost-effective video system for a rapid appraisal of deep-sea benthic habitats: the Azor drift-cam. Methods Ecol. Evol. 12 (8), 1379–1388.

Egbert, G.D., Erofeeva, S.Y., 2002. Efficient inverse modeling of barotropic ocean tides. J. Atmos. Ocean. Technol. 19 (2), 183–204.

Ekman, V.W., 1905. On the Influence of the Earth's Rotation on ocean-currents.

Escobar, C.A., Alvarez, D.R., 2023. Estimation of global ocean surface winds blending reanalysis, satellite and buoy datasets. Remote Sens. Appl.: Society and Environment 32, 101012.

Fukuba, Tatsuhiro, et al., 2018. Lander observatory with non-contact power supply and communication interfaces for long-term ecosystem monitoring in deep-sea. ISOPE International Ocean and Polar Engineering Conference. ISOPE.

García Molinos, J., Burrows, M.T., Poloczanska, E.S., 2017. Ocean currents modify the coupling between climate change and biogeographical shifts. Sci. Rep. 7 (1), 1332.

Garrett, C., Maas, L., 1993. Tides and their effects. Oceanus 36 (1), 27–37.

Giddens, J., Turchik, A., Goodell, W., Rodriguez, M., Delaney, D., 2021. The national geographic society deep-sea camera system: a low-cost remote video survey instrument to advance biodiversity observation in the deep ocean. Front. Mar. Sci. 7, 601411.

González-Pola, C., Sánchez Delgado, F., 2021. LanderPick, a remote operated trawled vehicle to cost -effectively deploy and recover lightweight oceanographic landers. In: 9th International Workshop on Marine Technology (MARTECH 2021). "Instrumentation Viewpoint", pp. 70–71 núm. 21, DLB.32814 -2006. ISSN1886 -4864. http://hdl.handle.net/2117/356433.

Gould, J., Sloyan, B., Visbeck, M., 2013. In situ ocean observations: a brief history, present status, and future directions. Int. Geophys. 103, 59–81.

Håland, E., Flekkøy, E.G., Måløy, K.J., 2012. Vertical and horizontal components of the electric background field at the sea bottom. Geophysics 77 (1), E1–E8.

Hardy, K., Kontoes, C., 2019. Application of small, untethered ocean landers for current, wave, and turbulence measurements. In: 2019 IEEE/OES Twelfth Current, Waves and Turbulence Measurement (CWTM). IEEE, pp. 1–4.

Harris, Catriona M., et al., 2018. Marine mammals and sonar: dose-response studies, the risk-disturbance hypothesis and the role of exposure context. J. Appl. Ecol. 55 (1), 396–404.

Heddleson, et al., 1957. Summary of Drag Coefficients of Various Shaped Cylinders.

Heffler, D.E., Locke, D.R., 1977. A deep ocean release mechanism. Mar. Geophys. Res. 3 (2), 229–232.

Hersbach, H., Bell, B., Berrisford, P., Hirahara, S., Horányi, A., Muñoz-Sabater, J., et al., 2020. The ERA5 global reanalysis. Q. J. Roy. Meteorol. Soc. 146 (730), 1999–2049.

Huang, Chai-Cheng, Tang, Hung-Jie, Liu, Jin-Yuan, 2007. Modeling volume deformation in gravity-type cages with distributed bottom weights or a rigid tube-sinker. Aquac. Eng. 37 (2), 144–157.

Jamieson, Alan J., 2016. Landers: baited cameras and traps. Biological Sampling in the Deep Sea, pp. 228–259.

Jamieson, Alan J., et al., 2009. HADEEP: free-falling landers to the deepest places on Earth. Mar. Technol. Soc. J. 43 (5), 151–160.

Jamieson, Alan J., Boorman, Ben, Jones, Daniel OB., 2013. Deep-sea benthic sampling. Methods for the Study of Marine Benthos, pp. 285–347.

Kawsar, M.R.U., Youssef, S.A., Faisal, M., Kumar, A., Seo, J.K., Paik, J.K., 2015. Assessment of dropped object risk on corroded subsea pipeline. Ocean. Eng. 106, 329–340.

Kopte, Robert, Dierking, Jan, Schulz, Marco, Schütte, Florian, 2024. Shipboard ADCP current measurements (38 kHz) during RV MARIA S. MERIAN cruise MSM126. https://doi.org/10.1594/PANGAEA.971775. PANGAEA.

Lagerloef, G.S., Mitchum, G.T., Lukas, R.B., Niiler, P.P., 1999. Tropical Pacific near-surface currents estimated from altimeter, wind, and drifter data. J. Geophys. Res. 104 (C10). https://doi.org/10.1029/1999JC900197, 23,313–323,326.

Langlois, Tim, et al., 2006. Baited underwater video for assessing reef fish populations in marine reserves. Fisheries Newsletter-South Pacific Commission 118, 53.

Lewis, Matthew, et al., 2017. Characteristics of the velocity profile at tidal-stream energy sites. Renew. Energy 114, 258–272.

Liljebäck, P., Mills, R., 2017. Eelume: a flexible and subsea resident IMR vehicle. In: Oceans 2017-Aberdeen. IEEE, pp. 1–4.

Liu, K., Courtene-Jones, W., Wang, X., Song, Z., Wei, N., Li, D., 2020. Elucidating the vertical transport of microplastics in the water column: a review of sampling methodologies and distributions. Water Res. 186, 116403.

Madgwick, S.O., Harrison, A.J., Vaidyanathan, R., 2011. Estimation of IMU and MARG orientation using a gradient descent algorithm. In: 2011 IEEE International Conference on Rehabilitation Robotics, pp. 1–7.

Max, L., Nürnberg, D., Chiessi, C.M., Lenz, M.M., Mulitza, S., 2022. Subsurface ocean warming preceded Heinrich events. Nat. Commun. 13 (1), 4217.

Mellor, G.L., 1996. Introduction to Physical Oceanography. American Institute of Physics, New York.

Miller, J.L., 2017. Ocean currents respond to climate change in unexpected ways. Phys. Today 70 (1), 17–18.

Miwa, Tetsuya, et al., 2016. Underwater observatory lander for the seafloor ecosystem monitoring using a video system. 2016 Techno-Ocean (Techno-Ocean). IEEE.

Monteiro, J.G., Jiménez, J.L., Gizzi, F., Přikryl, P., Lefcheck, J.S., Santos, R.S., Canning-Clode, J., 2021. Novel approach to enhance coastal habitat and biotope mapping with drone aerial imagery analysis. Sci. Rep. 11 (1), 574.

Moritz, H., 2000. Geodetic reference system 1980. J. Geod. 74 (1), 128–133.

Muir, L., Roman, C., Casagrande, D., D'Hondt, S., 2021. The deep autonomous profiler (DAP), a platform for hadal profiling and water sample collection. J. Atmos. Ocean. Technol. 38 (10), 1833–1845.

Munson, Bruce R., Rothmayer, Alric P., Okiishi, Theodore H., 2012. Fundamentals of Fluid Mechanics. Wiley Global Education.

Peoples, L.M., Norenberg, M., Price, D., McGoldrick, M., Novotny, M., Bochdansky, A., Bartlett, D.H., 2019. A full-ocean-depth rated modular lander and pressure-retaining sampler capable of collecting hadal-endemic microbes under in situ conditions. Deep Sea Res. Oceanogr. Res. Pap. 143, 50–57.

Poisson, A., Brunet, C., Brun-Cottan, J.C., 1980. Density of standard seawater solutions at atmospheric pressure. Deep-Sea Res., Part A 27 (12), 1013–1028.

Radeta, M., et al., 2023. Lost in the deep? Performance evaluation of dead reckoning techniques in underwater environments. Proceedings of the ACM on Interactive, Mobile, Wearable and Ubiquitous Technologies 7 (2), 1–27.

Radeta, M., et al., 2024. TRITON—Open telemetry and location estimation for marine monitoring based on IoT and LoRa. IEEE J. Ocean. Eng. 50 (2), 1244–1258.

Radeta, M., et al., 2025. MARS: programmable multipurpose auto-release system for aquatic observations. Limnol Oceanogr. Methods 23 (6), 376–388, 2025.

Ramming, H.G., Kowalik, Z., 1980. Numerical Modelling of Marine Hydrodynamics. Elsevier.

Rápalo, L.M., Gomes Jr, M.N., Mendiondo, E.M., 2024. Developing an open-source flood forecasting system adapted to data-scarce regions: a digital twin coupled with hydrologic-hydrodynamic simulations. J. Hydrol. 644, 131929.

Rascle, N., Chapron, B., Molemaker, J., Nouguier, F., Ocampo-Torres, F.J., Osuna Cañedo, J.P., et al., 2020. Monitoring intense oceanic fronts using sea surface roughness: satellite, airplane, and in situ comparison. J. Geophys. Res., Oceans 125 (8) e2019JC015704.

Roemmich, D., 1983. The balance of geostrophic and Ekman transports in the tropical Atlantic Ocean. J. Phys. Oceanogr. 13 (8), 1534–1539.

Röhrs, J., Sutherland, G., Jeans, G., Bedington, M., Sperrevik, A.K., Dagestad, K.F., LaCasce, J.H., 2023. Surface currents in operational oceanography: key applications, mechanisms, and methods. Journal of Operational Oceanography 16 (1), 60–88.

Schaefer, Kurt M., Fuller, Daniel W., 2016. Methodologies for investigating oceanodromous fish movements: archival and pop-up satellite archival tags. An introduction to fish migration 251.

Schmid, 1969. Penetration of Objects into the Ocean Bottom.

Sessions, Meredith Herbert, Marshall, Phillip M., 1971. A Precision deep-sea Time Release. Scripps Institution of Oceanography.

Silva, Eduardo, et al., 2016. TURTLE-a robotic autonomous deep sea lander. OCEANS 2016 MTS/IEEE Monterey. IEEE.

Tai, J.H., Yang, K.C., Gawarkiewicz, G., 2017. Subtidal current structure and variability of the continental shelf and slope of the northern South China Sea. Terr. Atmos. Ocean Sci. 28 (3), 411–423.

Tuchen, Franz Philip, et al., 2022. Two decades of full-depth current velocity observations from a moored observatory in the central equatorial Atlantic at 0 N, 23 W. Front. Mar. Sci. 9, 910979.

Vallis, G.K., 2017. Atmospheric and Oceanic Fluid Dynamics. Cambridge University Press.

van Haren, Hans, et al., 2020. Deep caller for ocean acoustic releases. J. Atmos. Ocean. Technol. 37 (6), 1135–1137.

Veritas, D.N., 2010. DNV-RP-F107: Risk Assessment of Pipeline Protection. Det Norske Veritas, Oslo, Norway.

Wagner, T.J., Eisenman, I., Ceroli, A.M., Constantinou, N.C., 2022. How winds and ocean currents influence the drift of floating objects. J. Phys. Oceanogr. 52 (5), 907–916.

Way, B.S., Hosom, D.S., Ware, J.D., Trask, R.P., Allsup, G.P., 1996. Vector measuring current meter (VMCM) upgrade. OCEANS 96 MTS/IEEE Conference Proceedings. The Coastal Ocean-Prospects for the 21st Century 1, 120–124. IEEE.

Wijaya, S.K., 2018. Design of portable sea temperature and sea current measuring equipment. In: 2018 3rd International Seminar on Sensors, Instrumentation, Measurement and Metrology (ISSIMM). IEEE, pp. 21–24.

Xiang, G., Wang, S., Soares, C.G., 2020. Study on the motion of a freely falling horizontal cylinder into water using OpenFOAM. Ocean. Eng. 196, 106811.

Yang, L., Zhao, S., Wang, X., et al., 2022. Deep-sea underwater cooperative operation of manned/unmanned submersible and surface vehicles for different application scenarios. J. Mar. Sci. Eng. 10 (7), 909.

Yasseri, S., 2014. Experiment of free-falling cylinders in water. Underw. Technol. 32 (3), 177–191.

Yin, A., Daeffler, M., Shomberg, R., Licht, S., Phillips, B., 2024. A predictable design and production workflow for field deployable underwater soft actuator applications. In: OCEANS 2024-Singapore. IEEE, pp. 1–8.

Yu, Zhou, et al., 2022. Dynamic analysis of bottom subsidence of benthic lander. J. Mar. Sci. Eng. 10 (6), 824.

Zhang, et al., 2023. Analysis of the Descent Process and Multi-Objective Optimization Design of a Benthic Lander.